Fluorine-Induced Aggregate-Interlocking for Color-Tunable Organic Afterglow with Simultaneously Improved Efficiency and Lifetime

Hui Li^{+}, Huanhuan Li^{+}, Jie Gu, Fei He, Hao Peng, Ye Tao,* Dan Tian, Qingqing Yang, Ping Li, Chao Zheng,* Wei Huang and Runfeng Chen*

Ms. H. Li, Dr. H. H. Li, Ms. J. Gu, Mr. F. He, Mr. H. Peng, Prof. Y. Tao, Ms. Q. Q. Yang, Dr. P. Li, Dr. C. Zheng, Prof. W. Huang and Prof. R. F. Chen
Key Laboratory for Organic Electronics and Information Displays & Jiangsu Key Laboratory for Biosensors, Institute of Advanced Materials (IAM), Nanjing University of Posts & Telecommunications, 9 Wenyuan Road, Nanjing 210023, China.
E-mail: iamytao@njupt.edu.cn, iamczheng@njupt.edu.cn and iamrfchen@njupt.edu.cn;

Dr. D. Tian
College of Materials Science and Engineering, Nanjing Forestry University, Nanjing 210037, China.

Prof. W. Huang
Frontiers Science Center for Flexible Electronics, Xi'an Institute of Flexible Electronics (IFE) and Xi'an Institute of Biomedical Materials & Engineering, Northwestern Polytechnical University (NPU), 127 West Youyi Road, Xi'an 710072, China.

$^{+}$These authors contributed equally to this work.

Content

1. Synthesis and characterization

Materials: All reagents, unless otherwise specified, were purchased from Aldrich, Acros or Alfa Aesar, and used without further purification. Manipulations involving air-sensitive reagents were performed in an atmosphere of dry argon (Ar).

Instruments: ^{1}H and ^{13}C-nuclear magnetic resonance (NMR) spectra were recorded on Bruker Ultra Shield Plus 400 MHz instruments with DMSO-d_6 as the solvents and tetramethylsilane (TMS) as the internal standard. High resolution mass spectra (HRMS) were collected by a LCT Premier XE (Waters) HRMS spectrometry. High-performance liquid chromatogram (HPLC) spectra were collected by an Agilent 1100 spectrometry *via* monitoring the onset absorption at 346 nm.

Materials Purification: To exclude the influence of isomer impurity on the afterglow performance, **POCz** and ***o*/*m*/*p*-FPOCz** crystals were carefully purified by column and recrystallized in a mixed dichloromethane and ethanol solution, and then further purified by sublimation.

Synthesis of (9*H*-carbazol-9-yl)(phenyl) methanone (POCz)

Carbazole (5.0 g, 30 mmol), sodium hydride (1.4 g, 36 mmol) and N, N-dimethylformamide (DMF) (50 mL) were mixed and stirred for 1.5 h under Ar atmosphere at room temperature. Subsequently, benzoyl chloride (5.1 g, 36 mmol) was rapidly added to the reaction mixture at room temperature. After stirring at room temperature for 12 h, the reaction was quenched by 10 mL water, and extracted with dichloromethane (3 × 200 mL). The organic layers were collected and dried with anhydrous sodium sulfate (Na_2SO_4) and purified by column chromatography to give **POCz**. Yield: 6.5 g of white powder (80%). ^{1}H NMR (400 MHz, DMSO-d_6, ppm): δ 8.23-8.21 (m, 2H), 7.76-7.71 (m, 3H), 7.63-7.60 (m, 2H), 7.42-7.37 (m, 6H); ^{13}C NMR (100 MHz, DMSO-d_6, ppm): δ 169.06, 138.48, 135.43, 132.51, 129.09, 128.57, 126.90, 125.41, 123.53, 120.37, 115.28. HRMS (EI): m/z calcd. for $C_{19}H_{14}NO$, 272.1075 $[M+H]^+$; found: 272.1073.

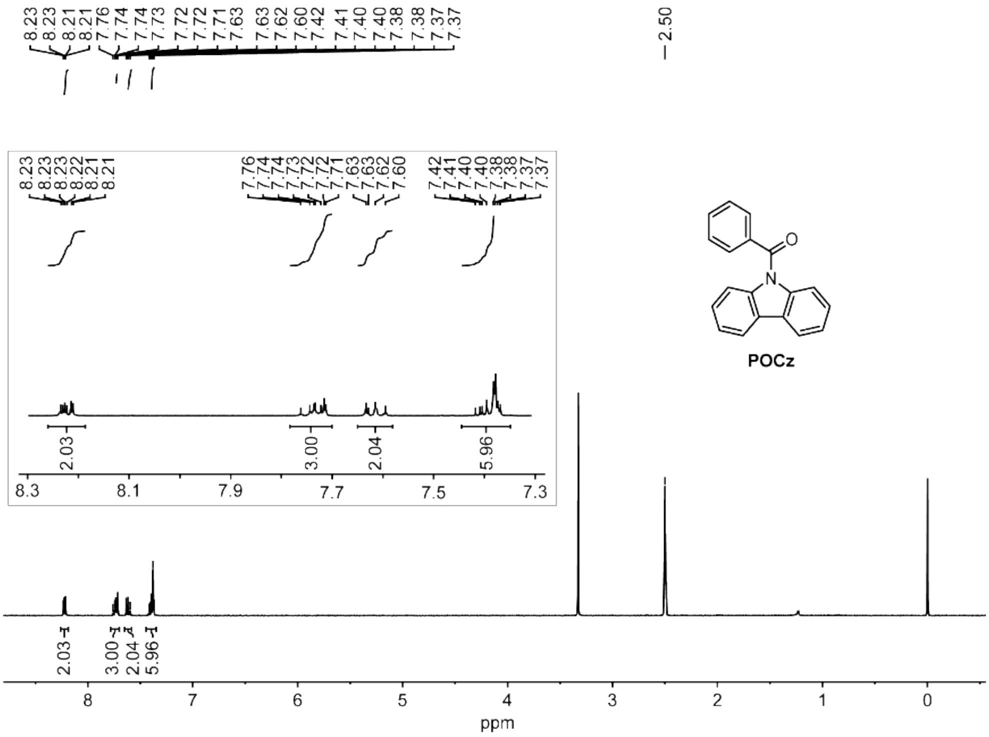

Figure S1. ^{1}H NMR spectrum of **POCz**.

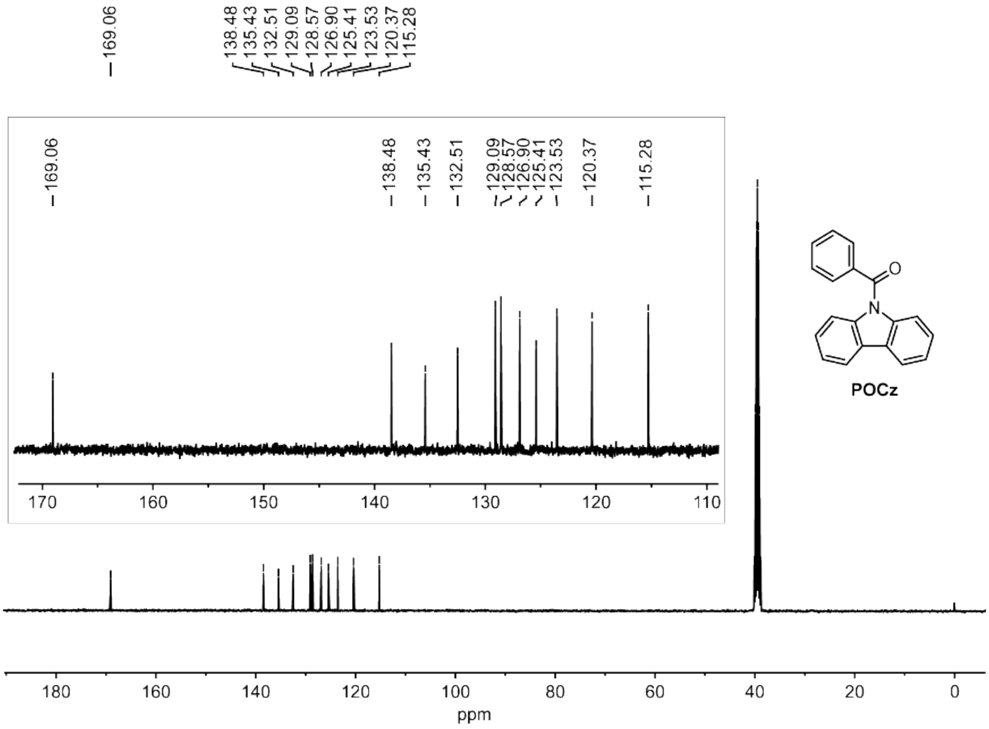

Figure S2. ^{13}C NMR spectrum of **POCz**.

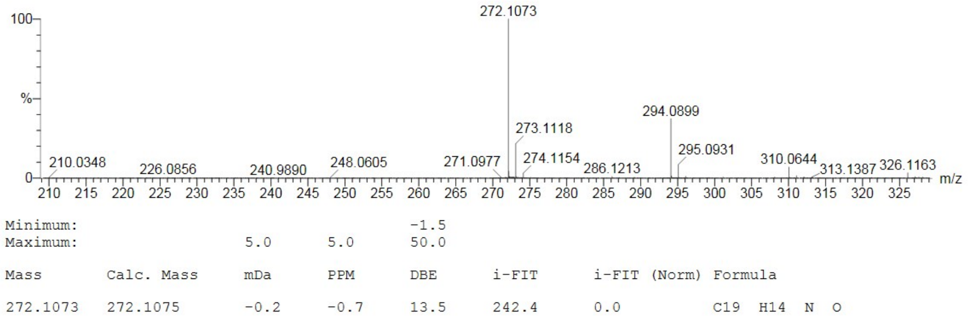

```
Minimum:                                      -1.5
Maximum:                  5.0        5.0      50.0

Mass        Calc. Mass    mDa        PPM      DBE       i-FIT       i-FIT (Norm) Formula

272.1073    272.1075      -0.2       -0.7     13.5      242.4       0.0          C19  H14  N  O
```

Figure S3. HRMS of **POCz**.

Synthesis of (9*H*-carbazol-9-yl)(2-fluorophenyl) methanone (*o*-FPOCz)

***o*-FPOCz** was prepared under the identical synthetic conditions described in the preparation of **POCz** using carbazole (5.0 g, 30 mmol), sodium hydride (1.4 g, 36 mmol), DMF (50 mL) and 2-fluorobenzoyl chloride (5.7 g, 36 mmol). Yield: 7.0 g of white powder (81%). ^{1}H NMR (400 MHz, DMSO-d_6, ppm): δ 8.23-8.21 (m, 2H), 7.84-7.76 (m, 2H), 7.52-7.37 (m, 8H); ^{13}C NMR (100 MHz, DMSO-d_6, ppm): δ 164.78, 160.08, 157.61, 138.43, 134.66, 130.36, 127.90, 126.28, 124.72, 120.99, 117.21, 117.01, 115.39. HRMS (EI): m/z calcd. for $C_{19}H_{13}NOF$, 290.0981 [M+H]$^+$; found: 290.0971.

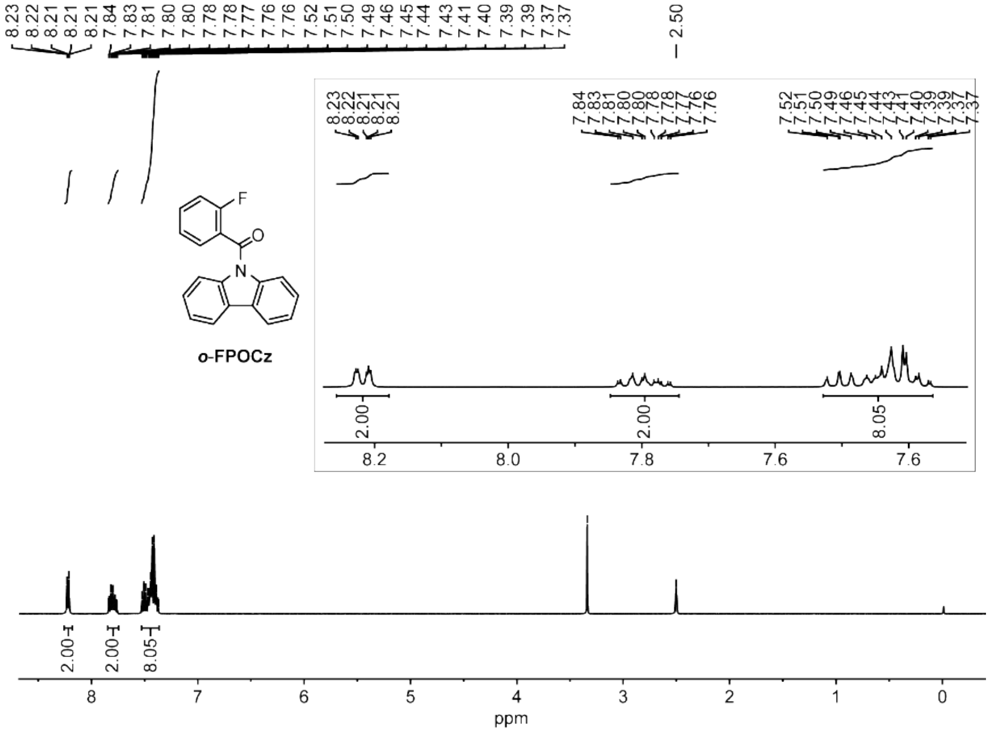

Figure S4. ^{1}H NMR spectrum of ***o*-FPOCz**.

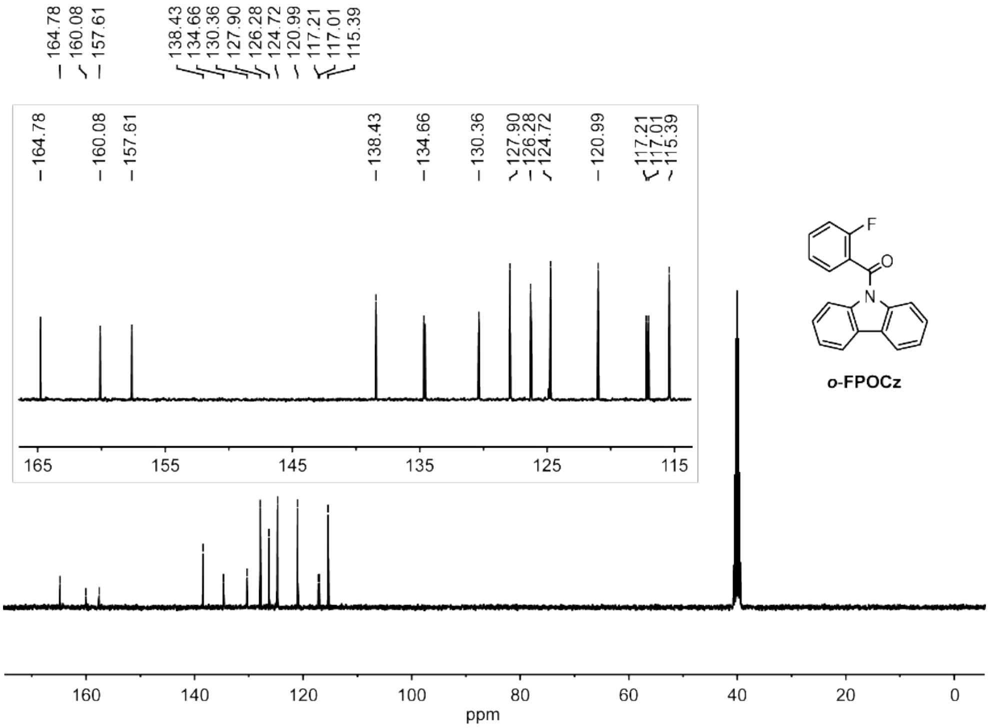

Figure S5. ^{13}C NMR spectrum of ***o*-FPOCz**.

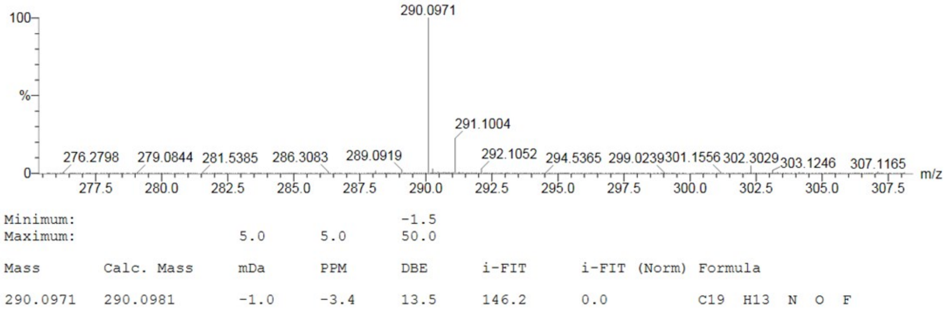

```
Minimum:                                    -1.5
Maximum:                   5.0      5.0     50.0

Mass      Calc. Mass     mDa      PPM      DBE     i-FIT      i-FIT (Norm) Formula

290.0971  290.0981       -1.0     -3.4     13.5    146.2      0.0          C19  H13  N  O  F
```

Figure S6. HRMS of ***o*-FPOCz**.

Synthesis of (9H-carbazol-9-yl)(3-fluorophenyl) methanone (*m*-FPOCz)

***m*-FPOCz** was prepared under the identical synthetic conditions described in the preparation of **POCz** using carbazole (5.0 g, 30 mmol), sodium hydride (1.4 g, 36 mmol), DMF (50 mL) and 3-fluorobenzoyl chloride (5.7 g, 36 mmol). Yield: 7.2 g of white powder (83%). ^{1}H NMR (400 MHz, DMSO-d_6, ppm): δ 8.22-8.20 (m, 2H), 7.66-7.54 (m, 4H), 7.41-7.39 (m, 6H); ^{13}C NMR (100 MHz, DMSO-d_6, ppm): δ 168.09, 163.77, 161.32, 138.85, 138.12, 131.89, 127.50, 126.08, 125.12, 124.24, 120.87, 119.86, 115.88. HRMS (EI): m/z calcd. for $C_{19}H_{13}NOF$, 290.0981 $[M+H]^+$; found: 290.0975.

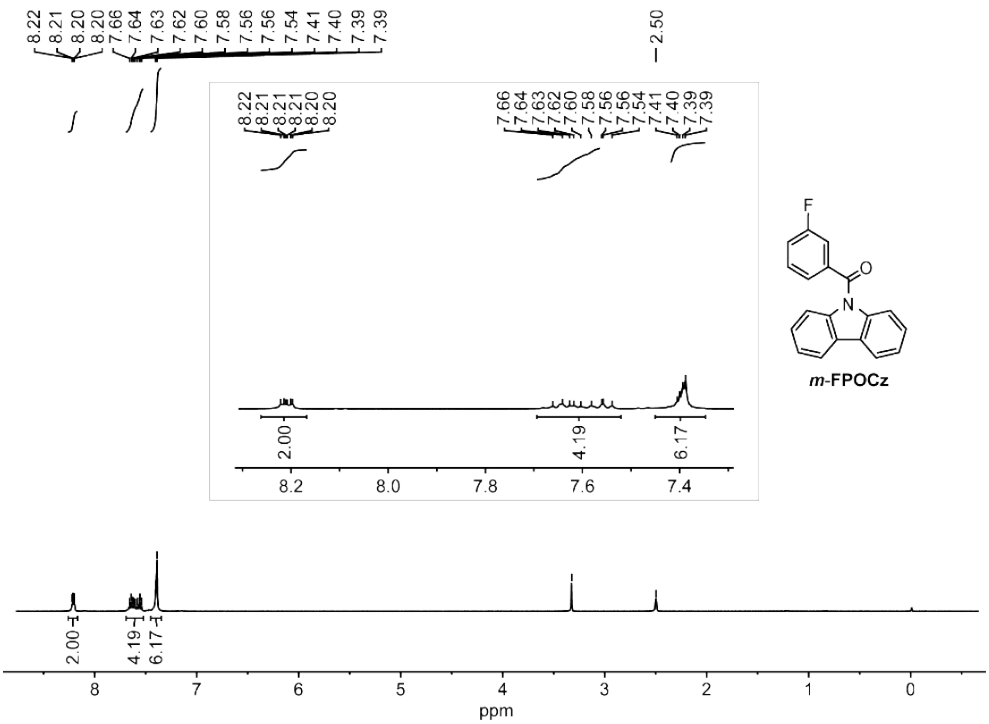

Figure S7 ^{1}H NMR spectrum of ***m*-FPOCz**.

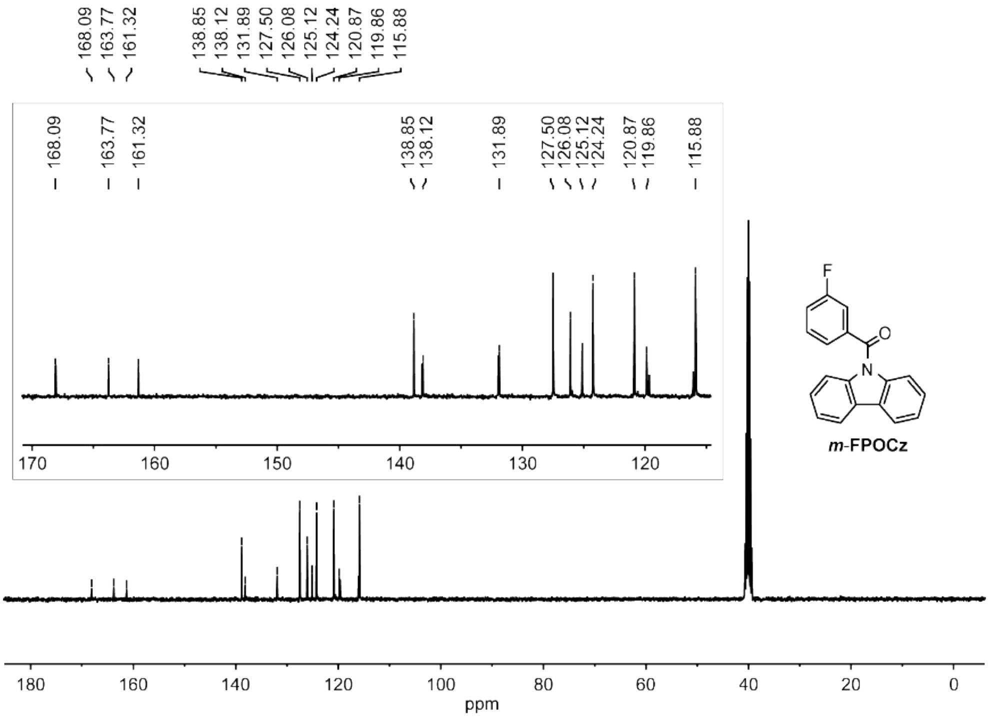

Figure S8. ^{13}C NMR spectrum of ***m*-FPOCz**.

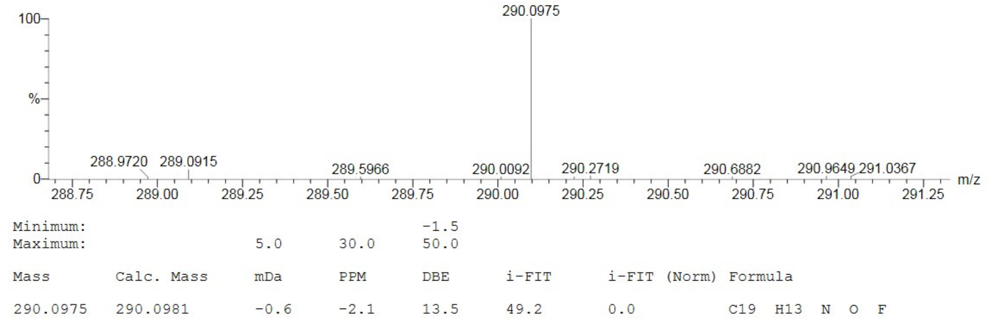

```
Minimum:                                    -1.5
Maximum:                 5.0       30.0     50.0

Mass       Calc. Mass    mDa       PPM      DBE       i-FIT      i-FIT (Norm) Formula

290.0975   290.0981      -0.6      -2.1     13.5      49.2       0.0          C19  H13  N  O  F
```

Figure S9. HRMS of ***m*-FPOCz**.

Synthesis of (9H-carbazol-9-yl)(4-fluorophenyl) methanone (*p*-FPOCz)

***p*-FPOCz** was prepared under the identical synthetic conditions described in the preparation of **POCz** using carbazole (5.0 g, 30 mmol), sodium hydride (1.4 g, 36 mmol), DMF (50 mL) and 4-fluorobenzoyl chloride (5.7 g, 36 mmol). Yield: 7.4 g of white powder (85%). ^{1}H NMR (400 MHz, DMSO-d_6, ppm): δ 8.24-8.20 (m, 2H), 7.84-7.80 (m, 2H), 7.47-7.38 (m, 8H); ^{13}C NMR (100 MHz, DMSO-d_6, ppm): δ 168.47, 166.17, 163.67, 138.98, 132.27, 127.43, 125.90, 124.02, 120.87, 116.83, 115.75. HRMS (EI): m/z calcd. for $C_{19}H_{13}NOF$, 290.0981 [M+H]$^+$; found: 290.0974.

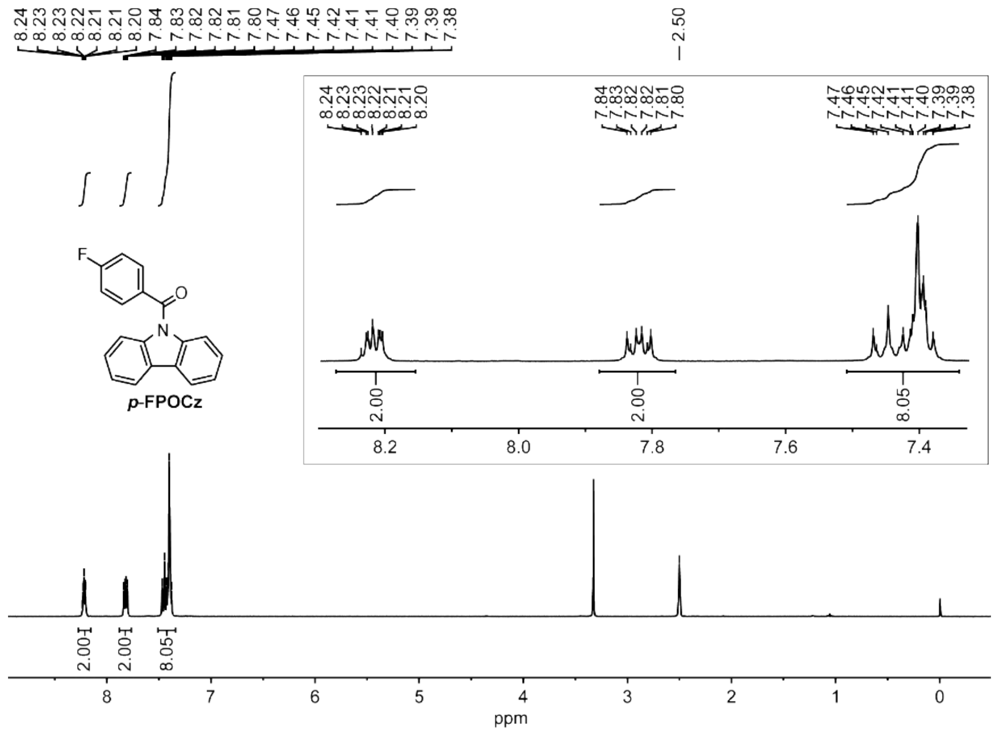

Figure S10. ^{1}H NMR spectrum of ***p*-FPOCz**.

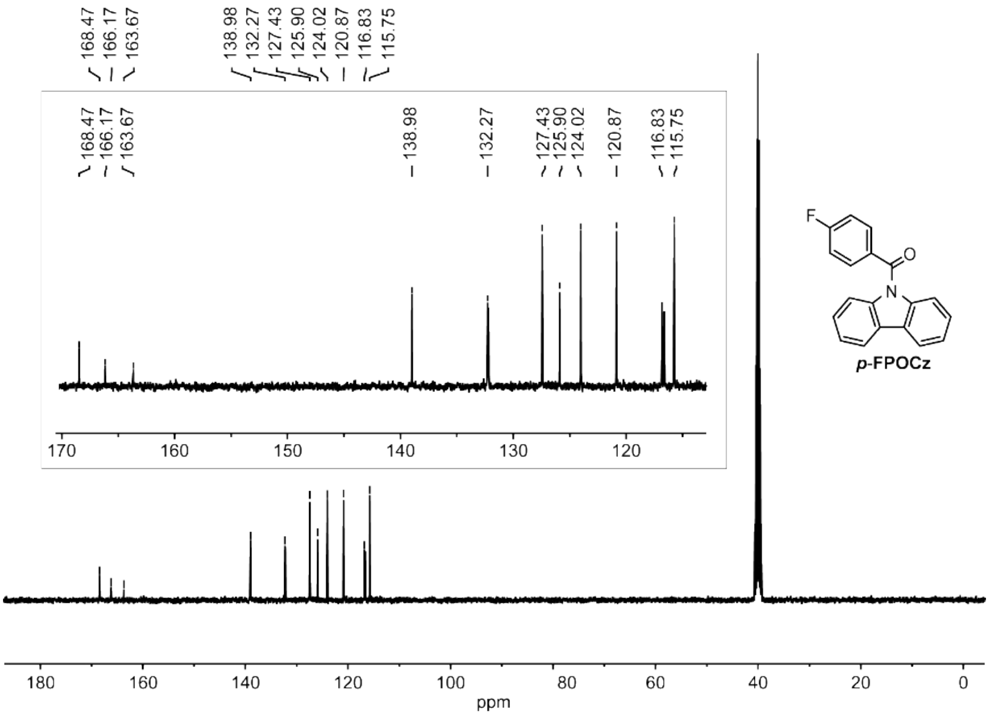

Figure S11. ^{13}C NMR spectrum of ***p*-FPOCz**.

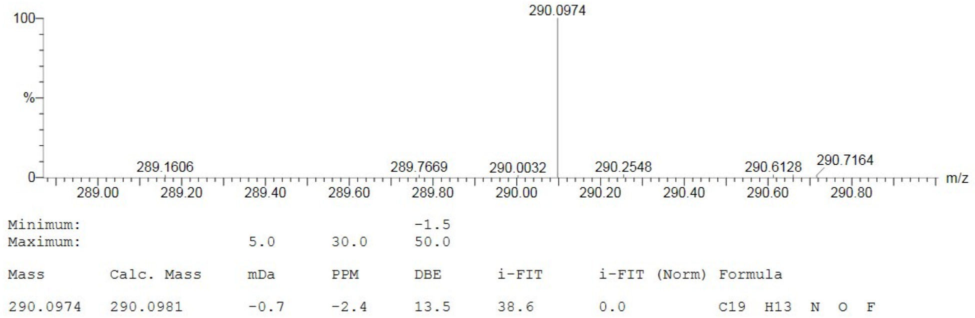

```
Minimum:                                        -1.5
Maximum:                        5.0      30.0   50.0

Mass      Calc. Mass    mDa      PPM     DBE      i-FIT     i-FIT (Norm) Formula

290.0974  290.0981      -0.7     -2.4    13.5     38.6      0.0          C19  H13  N  O  F
```

Figure S12. HRMS of ***p*-FPOCz**.

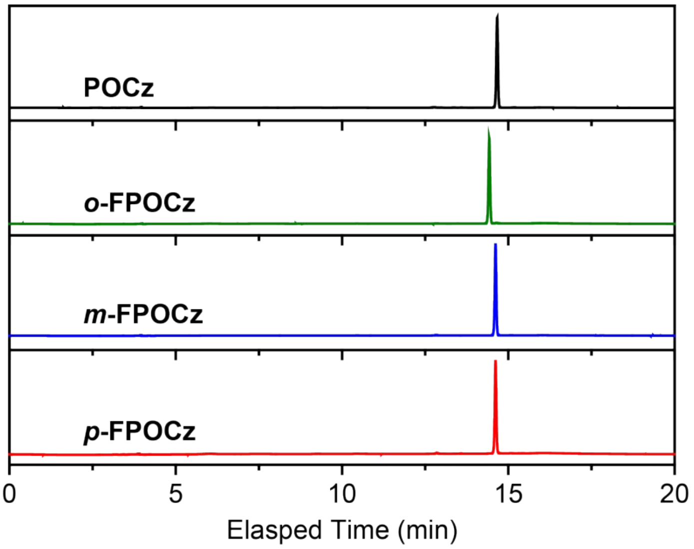

Figure S13. HPLC spectra of **POCz** and ***o*/*m*/*p*-FPOCz**.

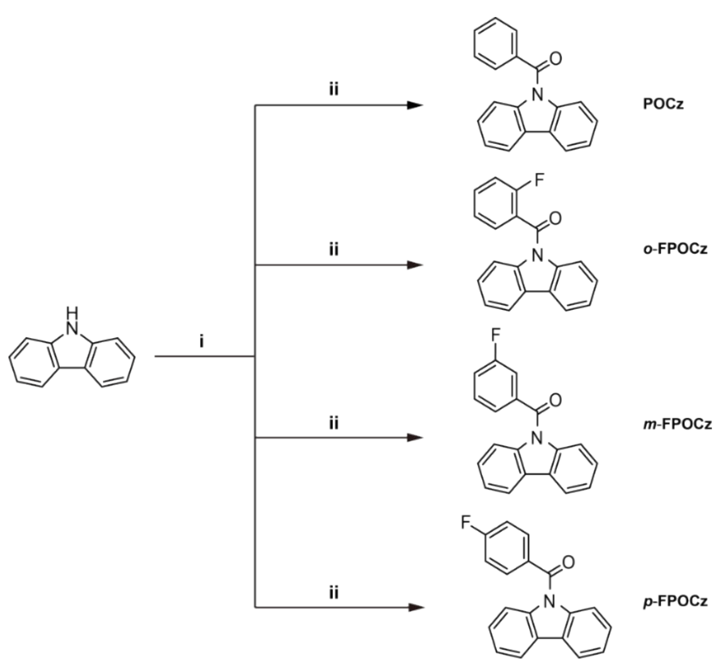

Scheme S1. Synthetic route of **POCz**, ***o*-FPOCz**, ***m*-FPOCz** and ***p*-FPOCz**. (i) 1.2 equiv. NaH, DMF, room temperature, 1.5 h; (ii) 1.2 equiv. benzoyl chloride (for **POCz**), 2-fluorobenzoyl chloride (for ***o*-FPOCz**), 3-fluorobenzoyl chloride (for ***m*-FPOCz**) or 4-fluorobenzoyl chloride (for ***p*-FPOCz**), room temperature, 12 h.

2. Thermal properties

Thermogravimetric analyses (TGA) were conducted on a DTG-60 Shimadzu thermal analyst system under a heating rate of 10ºC/min and a nitrogen flow rate of 50 cm^3/min. The differential scanning calorimetry (DSC) analyses were performed on a Shimadzu DSC-60A instrument under a heating rate of 10ºC/min and a nitrogen flow rate of 20 cm^3/min.

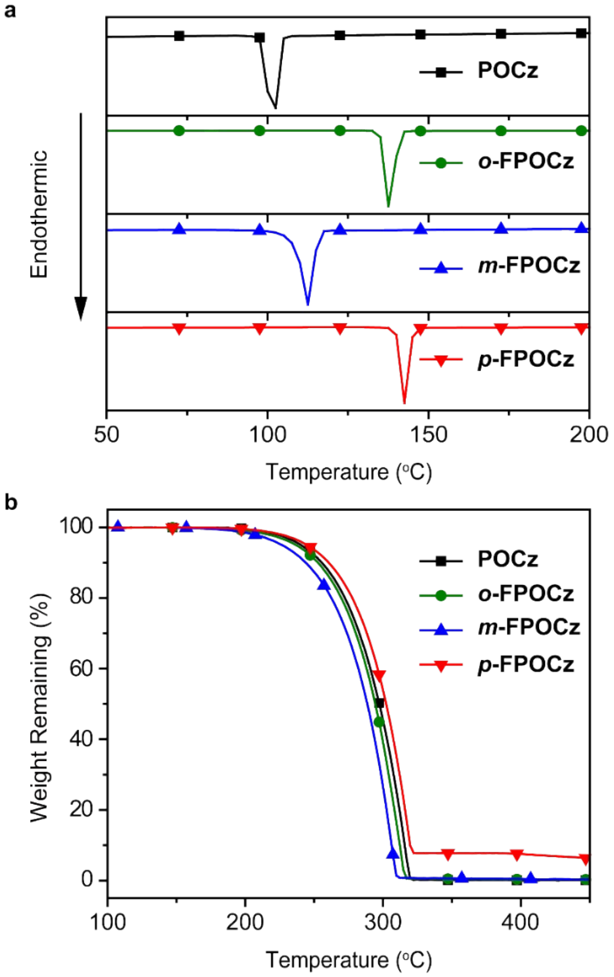

Figure S14. DSC (a) and TGA (b) curves of **POCz**, ***o*-FPOCz**, ***m*-FPOCz** and ***p*-FPOCz**.

3. Photophysical investigations

Ultraviolet/visible (UV/Vis) and fluorescence spectra were recorded on a Jasco V-750 spectrophotometer and Edinburgh FLS980, respectively. The absolute photoluminescence quantum yield (PLQY) was obtained using an Edinburgh FLS980 fluorescence spectrophotometer equipped with an integrating sphere. For fluorescence decay measurements, picosecond pulsed light-emitting diode (EPLED-380, wavelength: 377 nm, pulse width: 947.7 ps; EPLED-295, wavelength: 300 nm, pulse width: 833.7 ps) were used. Phosphorescence spectra were obtained using an Edinburgh FLS980 fluorescence spectrophotometer at 77 K with a 10 ms delay time after excitation using a microsecond flash lamp. The microsecond flash lamp produces short, typically a few μs, and high irradiance optical pulses for phosphorescence decay measurements in the range from microseconds to seconds. The kinetic measurements, afterglow spectra and ultralong lifetimes were also measured using an Edinburgh FLS980 fluorescence spectrophotometer. Excitation-phosphorescence mapping was measured using Hitachi F-4700 with a 25 ms delay time under ambient condition. The lifetimes (τ) of the luminescence were obtained by fitting the decay curve with a multi-exponential decay function of

$$I(\mathrm{t}) = \sum_i A_i e^{-\frac{t}{\tau_i}}$$

where A_i and τ_i represent the amplitudes and lifetimes of the individual components for multi-exponential decay profiles, respectively.[1]

On the basis of the measured fluorescence and phosphorescence efficiencies and the emission lifetimes, the radiative and nonradiative decay rates, as well as intersystem crossing (ISC) rate can be calculated following the photophysical kinetic equations reported previously. The lifetime and photoluminescence quantum yield (PLQY) of fluorescence (τ^{F} and Φ^{F}), organic afterglow ($\tau^{\mathrm{T*}}$ and $\Phi^{\mathrm{T*}}$) and ISC (Φ^{ISC}) can be expressed in Equations (S1-5).

$$\tau^{\mathrm{F}} = \frac{1}{k_{\mathrm{r}}^{\mathrm{F}} + k_{\mathrm{nr}}^{\mathrm{F}} + k_{\mathrm{ISC}}} \tag{S1}$$

$$\Phi^{\mathrm{F}} = \frac{k_{\mathrm{r}}^{\mathrm{F}}}{k_{\mathrm{r}}^{\mathrm{F}} + k_{\mathrm{nr}}^{\mathrm{F}} + k_{\mathrm{ISC}}} = k_{\mathrm{r}}^{\mathrm{F}} \times \tau^{\mathrm{F}} \tag{S2}$$

$$\tau^{\mathrm{T}^*} = \frac{1}{k_{\mathrm{r}}^{\mathrm{T}^*} + k_{\mathrm{nr}}^{\mathrm{T}^*}} \tag{S3}$$

$$\Phi^{\mathrm{T}^*} = \Phi^{\mathrm{ISC}} \times \frac{k_{\mathrm{r}}^{\mathrm{T}^*}}{k_{\mathrm{r}}^{\mathrm{T}^*} + k_{\mathrm{nr}}^{\mathrm{T}^*}} = \Phi^{\mathrm{ISC}} \times k_{\mathrm{r}}^{\mathrm{T}^*} \times \tau^{\mathrm{T}^*} \tag{S4}$$

$$\Phi^{\mathrm{ISC}} = \frac{k_{\mathrm{ISC}}}{k_{\mathrm{r}}^{\mathrm{F}} + k_{\mathrm{nr}}^{\mathrm{F}} + k_{\mathrm{ISC}}} = k_{\mathrm{ISC}} \times \tau^{\mathrm{F}} \tag{S5}$$

One of the most important and experimentally elusive parameters is the rate constant for intersystem crossing from the lowest excited singlet to triplet state, k_{ISC}. Experimentally, k_{ISC} can be estimated as follows：

$$\frac{\Phi^{\mathrm{T}^*}}{\tau^{\mathrm{F}}} \leq k_{\mathrm{ISC}} \leq \frac{1-\Phi^{\mathrm{F}}}{\tau^{\mathrm{F}}} \tag{S6}$$

$$k_{\mathrm{ISC}}^{\min} = \frac{\Phi^{\mathrm{T}^*}}{\tau^{\mathrm{F}}} \tag{S7}$$

$$k_{\mathrm{ISC}}^{\max} = \frac{1-\Phi^{\mathrm{F}}}{\tau^{\mathrm{F}}} \tag{S8}$$

Among them, $k_{\mathrm{r}}^{\mathrm{F}}$ and $k_{\mathrm{nr}}^{\mathrm{F}}$ represent the radiative and non-radiative fluorescence rate constant respectively; $k_{\mathrm{r}}^{\mathrm{T}^*}$ and $k_{\mathrm{nr}}^{\mathrm{T}^*}$ are the radiative and non-radiative organic afterglow rate constant, respectively. Based on the obtained data and equations, $k_{\mathrm{r}}^{\mathrm{F}}$, $k_{\mathrm{nr}}^{\mathrm{F}}$, $k_{\mathrm{r}}^{\mathrm{T}^*}$ and $k_{\mathrm{nr}}^{\mathrm{T}^*}$ can be obtained by the following Equations (S9-12), respectively.

$$k_{\mathrm{r}}^{\mathrm{F}} = \frac{\Phi^{\mathrm{F}}}{\tau^{\mathrm{F}}} \tag{S9}$$

$$k_{\mathrm{nr}}^{\mathrm{F}} = \frac{1-\Phi^{\mathrm{F}}-\Phi^{\mathrm{ISC}}}{\tau^{\mathrm{F}}} \tag{S10}$$

$$k_{\mathrm{r}}^{\mathrm{T}^*} = \frac{\Phi^{\mathrm{T}^*}}{\Phi^{\mathrm{ISC}} \times \tau^{\mathrm{T}^*}} \tag{S11}$$

$$k_{\mathrm{nr}}^{\mathrm{T}^*} = \frac{1}{\tau^{\mathrm{T}^*}} - k_{\mathrm{r}}^{\mathrm{T}^*} \tag{S12}$$

The similar absorption and steady-state photoluminescence (SSPL) spectra of **POCz**, ***o*-FPOCz**, ***m*-FPOCz** and ***p*-FPOCz** were observed in dilute tetrahydrofuran (THF) solution (~ 10^{-5} mol L^{-1}), showing carbazole dominated absorption peaks at around 279, 305, and 316 nm and emission bands at 338, 354 nm, which demonstrate that the fluorine incorporation has limited influence on the photophysical properties at the single molecular state (**Figure S15**). The fluorescence character of these molecules in solution was verified by the typical nanosecond (ns) emission lifetime (**Figure S16**).

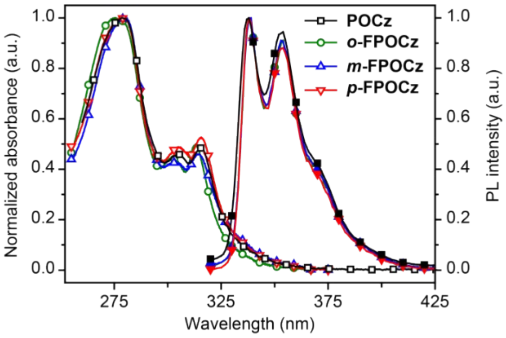

Figure S15. Absorption (open symbol) and SSPL (solid symbol) spectra of **POCz**, ***o*-FPOCz**, ***m*-FPOCz** and ***p*-FPOCz** in THF (~ 10^{-5} mol L^{-1}).

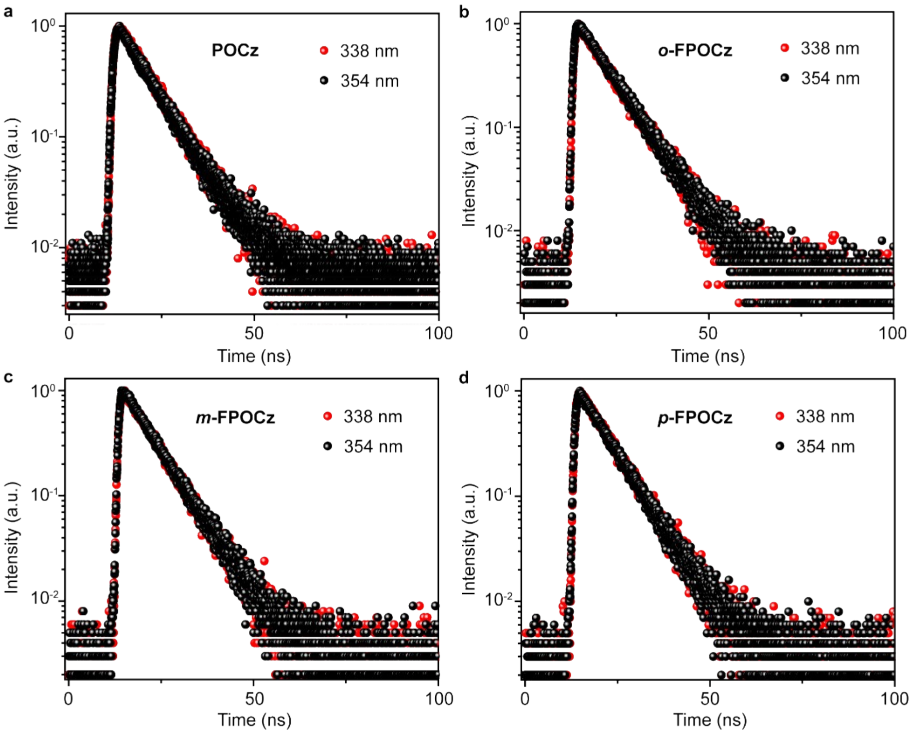

Figure S16. Fluorescence decay profiles of **POCz** (a), ***o*-FPOCz** (b), ***m*-FPOCz** (c) and ***p*-FPOCz** (d) in THF (~ 10^{-5} mol L^{-1}) excited by 300 nm UV light under ambient conditions.

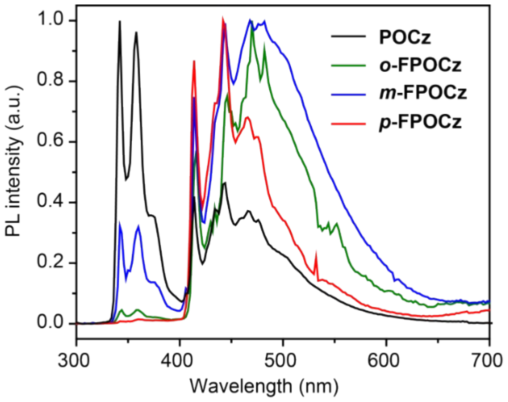

Figure S17. SSPL of **POCz**, ***o*-FPOCz**, ***m*-FPOCz** and ***p*-FPOCz** in THF (~ 10^5 mol L^{-1}) glass recorded at 77 K excited by 300 nm UV light.

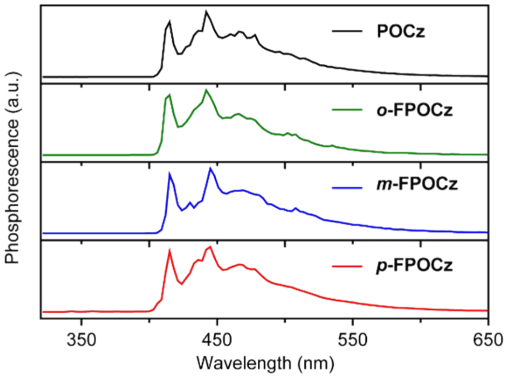

Figure S18. Phosphorescence spectra of **POCz**, ***o*-FPOCz**, ***m*-FPOCz** and ***p*-FPOCz** recorded at 77 K in THF (~ 10^{-5} mol L^{-1}) glass with a delay time of 10 ms and the excitation wavelength is 300 nm UV light.

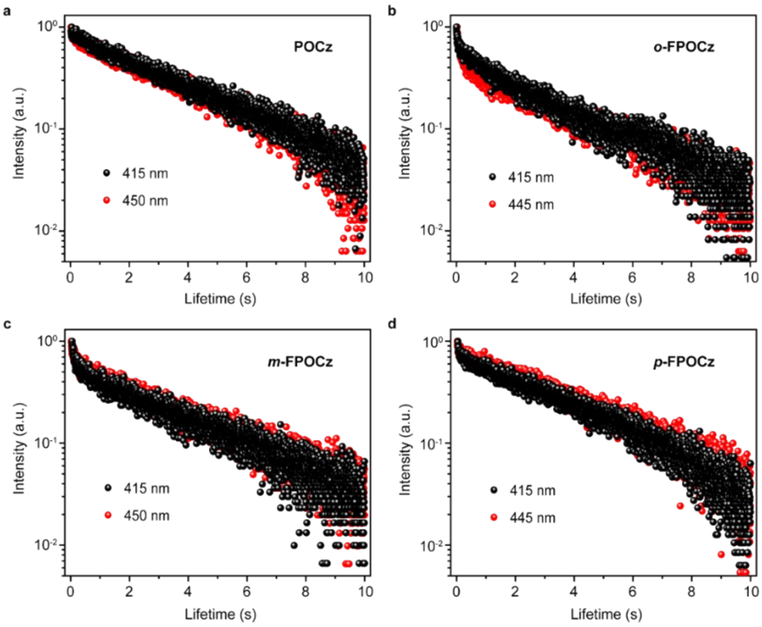

Figure S19. Phosphorescence decay profiles of **POCz** (a), ***o*-FPOCz** (b), ***m*-FPOCz** (c) and ***p*-FPOCz** (d) in THF (~ 10^{-5} mol L^{-1}) glass recorded at 77 K excited by 300 nm UV light.

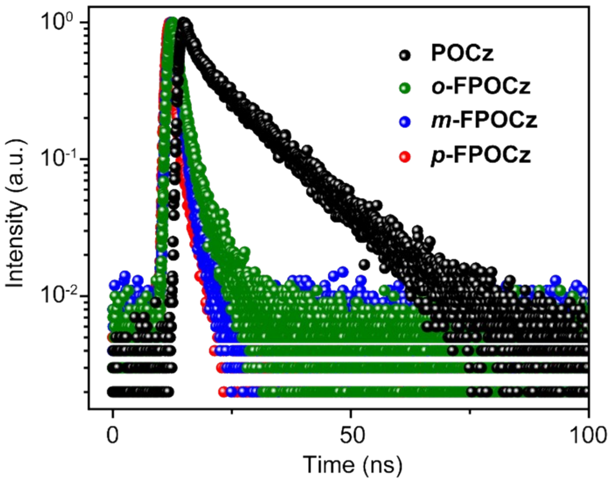

Figure S20. Fluorescence decay profiles of **POCz**, ***o*-FPOCz**, ***m*-FPOCz** and ***p*-FPOCz** crystals excited by 377 nm UV light under ambient conditions.

Table S1. Photoluminescence properties and kinetic parameters of organic afterglow molecules.[2, 3]

Parameters		**POCz**	***o*-FPOCz**	***m*-FPOCz**	***p*-FPOCz**
Fluorescence	λ [nm]	450	472	456	458
	τ^{F} [ns]	12.24	2.71	1.79	1.96
	Φ^{F} [%]	3.8	4.0	1.3	1.3
	k_r^{F} [s^{-1}]	3.07×10^{6}	1.46×10^{7}	7.37×10^{6}	6.58×10^{6}
	$k_{nr}{}^{F}{}_{max}$ [s^{-1}]	7.73×10^{7}	3.45×10^{8}	4.93×10^{8}	4.86×10^{8}
	$k_{nr}{}^{F}{}_{min}$ [s^{-1}]	0	0	0	0
ISC	ΔE_{ST} [eV]	0.64	0.64	0.64	0.64
	k_{ISC}^{max} [s^{-1}]	7.86×10^{7}	3.54×10^{8}	5.51×10^{8}	5.04×10^{8}
	k_{ISC}^{min} [s^{-1}]	1.32×10^{6}	9.70×10^{6}	5.84×10^{7}	1.73×10^{7}
Organic afterglow	λ [nm]	527, 572	527, 572	527, 572	527, 572
	τ^{T*} [s]	0.75	0.83	0.96	1.09
	Φ^{T*} [%]	1.6	2.6	10.5	3.4
	$k_r{}^{T*}{}_{max}$ [s^{-1}]	1.33	1.20	1.04	0.92
	$k_r{}^{T*}{}_{min}$ [s^{-1}]	2.23×10^{-2}	3.30×10^{-2}	1.10×10^{-1}	3.16×10^{-2}
	$k_{nr}{}^{T*}{}_{max}$ [s^{-1}]	1.31	1.17	0.93	0.89
	$k_{nr}{}^{T*}{}_{min}$ [s^{-1}]	0	0	0	0

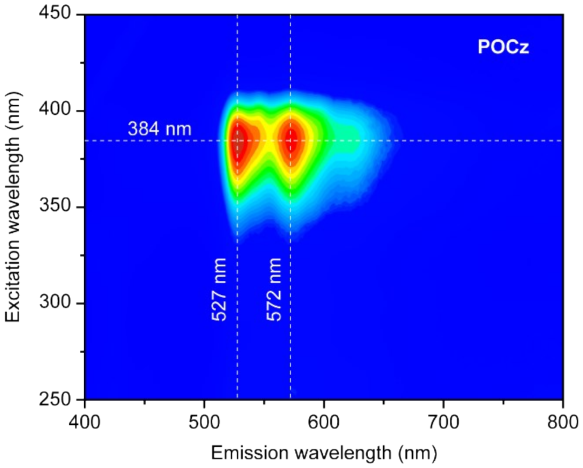

Figure S21. Excitation-phosphorescence mapping of **POCz** crystal with a delay time of 25 ms under ambient conditions.

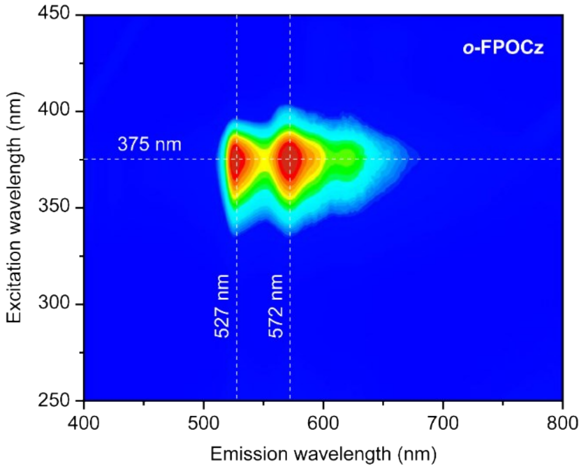

Figure S22. Excitation-phosphorescence mapping of ***o*-FPOCz** crystal with a delay time of 25 ms under ambient conditions.

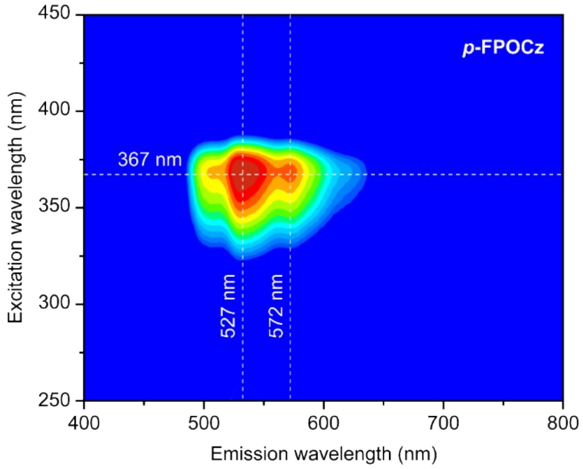

Figure S23. Excitation-phosphorescence mapping of ***p*-FPOCz** crystal with a delay time of 25 ms under ambient conditions.

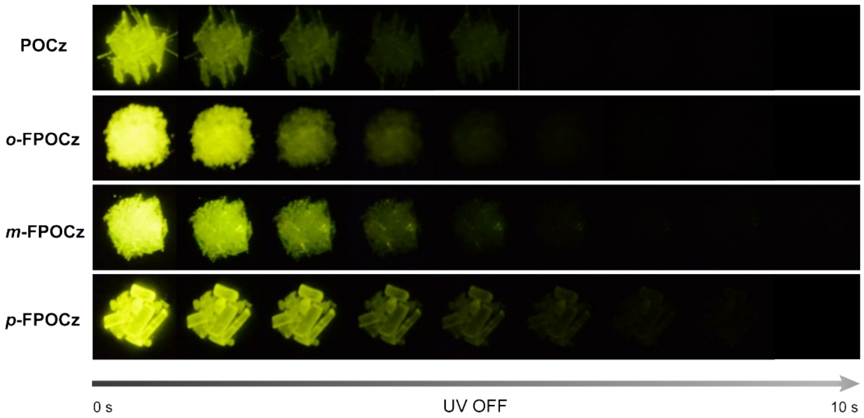

Figure S24. Photographs of **POCz** and ***o*/*m*/*p*-FPOCz** powders taken after the irradiation of a 365 nm UV lamp under ambient conditions.

To systemically investigate the influence of excitation intensity and duration on the organic afterglow properties, the intensities of organic afterglow emission were measured through kinetic analyses. As indicated in **Figure S25**, the excitation light at 365 nm with varied intensity was turned on at 5 s, maintained for 10 s, and then turned off. By increasing excitation intensity, both steady-state and afterglow emission were significantly strengthened. Notably, the organic afterglow emission keeps stable during the excitation for 10 s and then slowly decay in mono-exponential manner after ceasing the excitation light at 15 s, suggesting the ultralong lifetime. The influences of excitation duration on the afterglow emission were studied by detecting its intensity of corresponding emission band through varying irradiating time of the excitation light (**Figure S26**). The steady-state and afterglow emission intensities greatly increased and become almost constant when the excitation duration varies from 0.01 to 10 s. Taken together, the afterglow emission can be effectively excited by low intensity (**Figure S25**) and short irradiation time (**Figure 26**) of excitation light under ambient conditions.

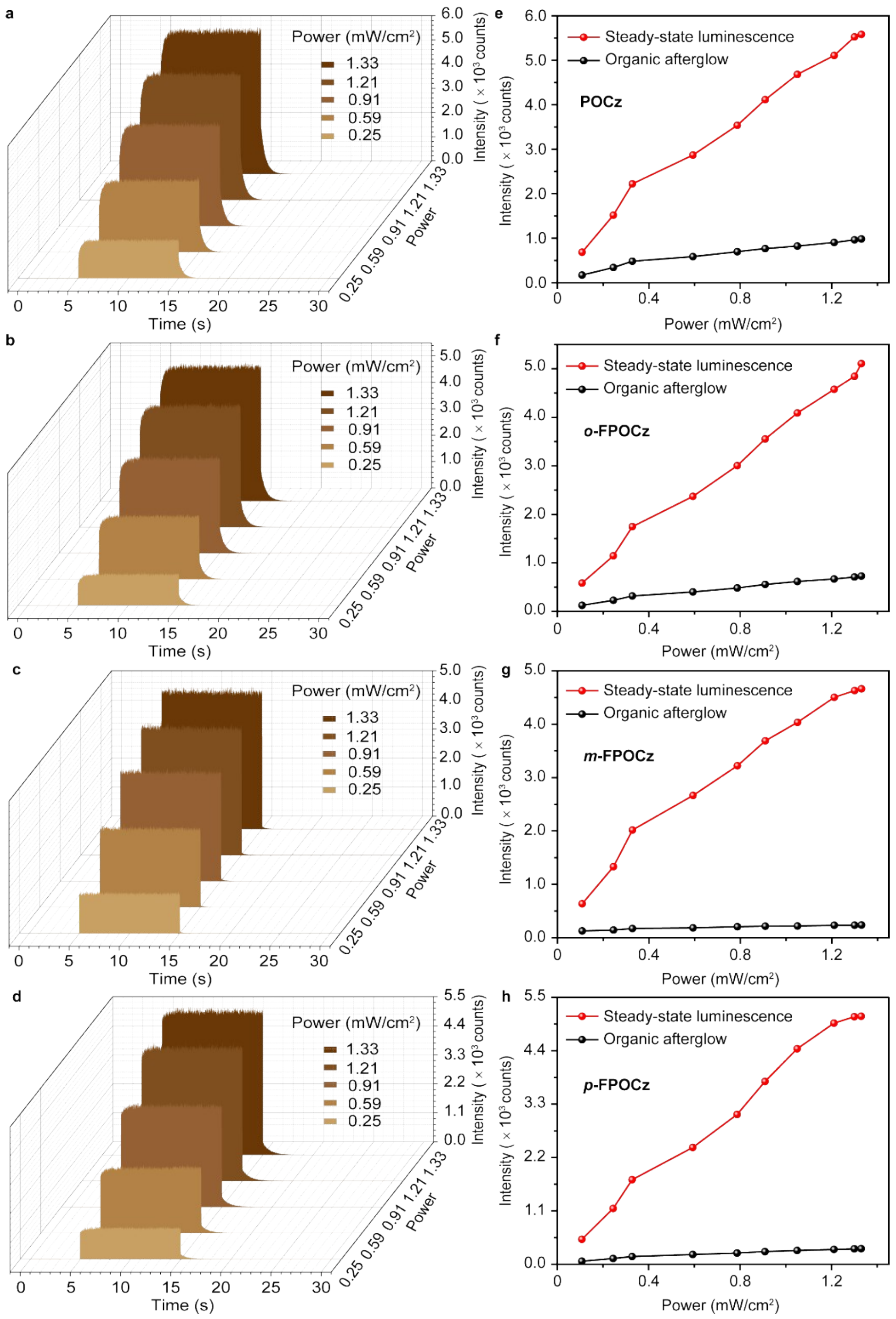

Figure S25. (a-d) Photoluminescence intensity profiles of 527 nm emission peak of **POCz** (a), ***o*-FPOCz** (b), ***m*-FPOCz** (c) and ***p*-FPOCz** (d) crystals. (e-h) SSPL (red) and organic afterglow (black) intensities at 527 nm (e-h) as a function of time and power excited by 365 nm under ambient conditions.

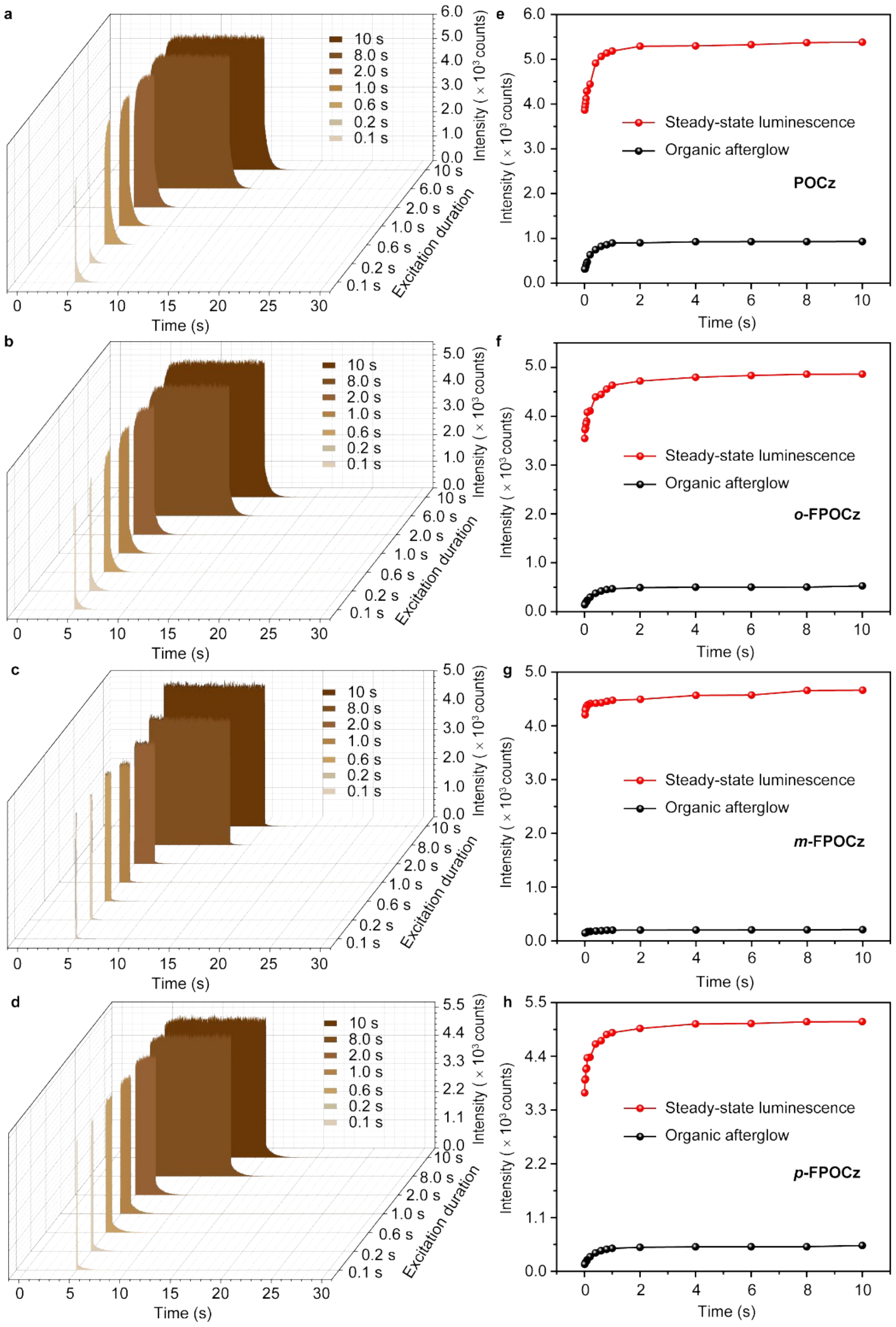

Figure S26. (a-d). Photoluminescence intensity profiles of 527 nm emission of **POCz** (a), ***o*-FPOCz** (b), ***m*-FPOCz** (c) and ***p*-FPOCz** (d) crystals. (e-h). SSPL (red) and organic afterglow (black) intensities at 527 nm as a function of time upon 365 nm excitation with different irradiating time (0.01 ~ 10 s) under ambient conditions.

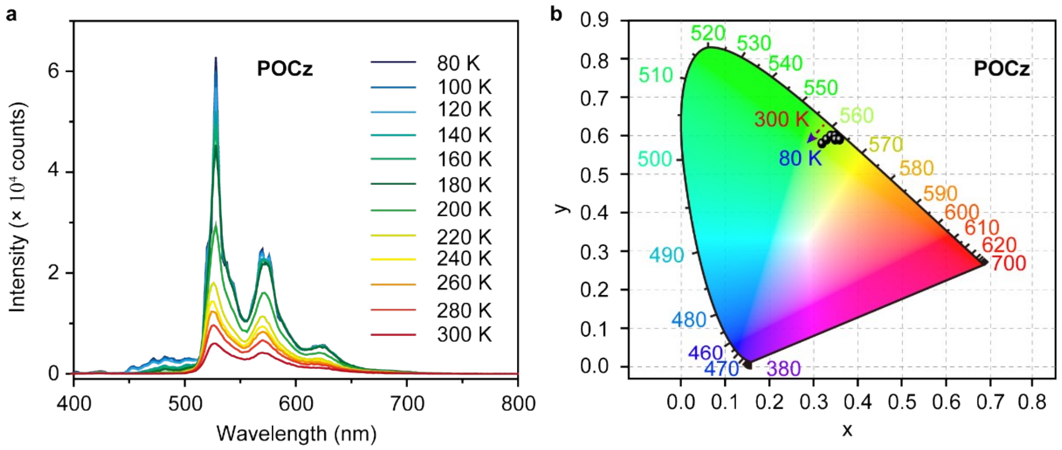

Figure S27. (a). Temperature-dependent afterglow spectra of **POCz** crystal from 300 to 80 K. (b). CIE 1931 coordinates of afterglow emission of **POCz** crystal from 300 to 80 K.

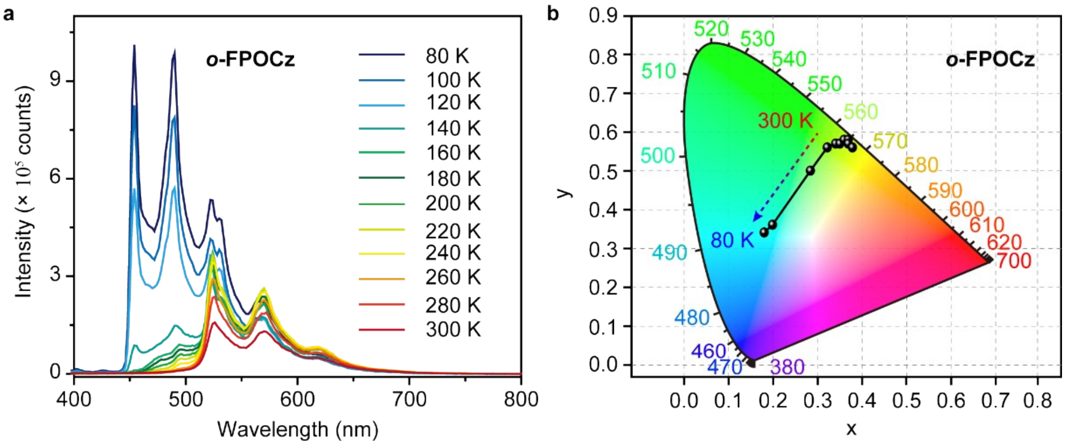

Figure S28. (a). Temperature-dependent afterglow spectra of ***o*-FPOCz** crystal from 300 to 80 K. (b). CIE 1931 coordinates of afterglow emission of ***o*-FPOCz** crystal from 300 to 80 K.

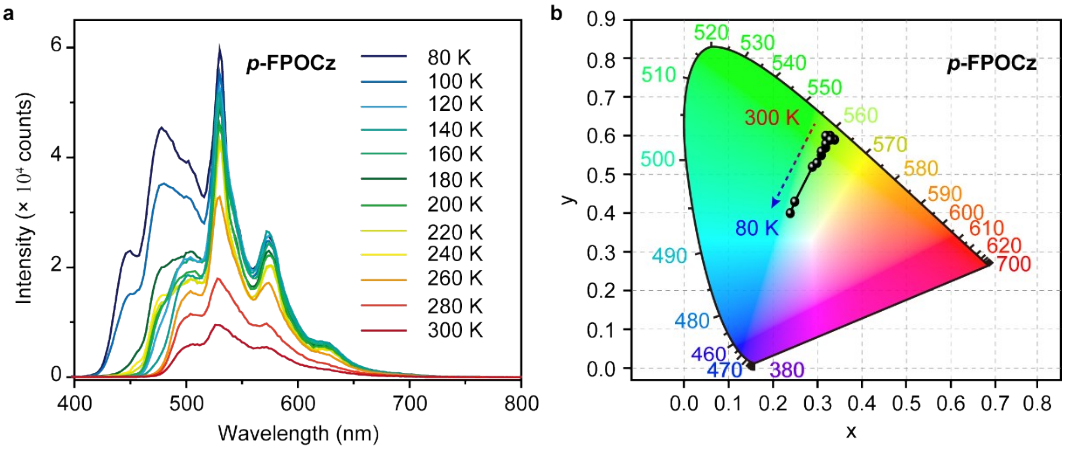

Figure S29. (a). Temperature-dependent afterglow spectra of ***p*-FPOCz** crystal from 300 to 80 K. (b). CIE 1931 coordinates of afterglow emission of ***p*-FPOCz** crystal from 300 to 80 K.

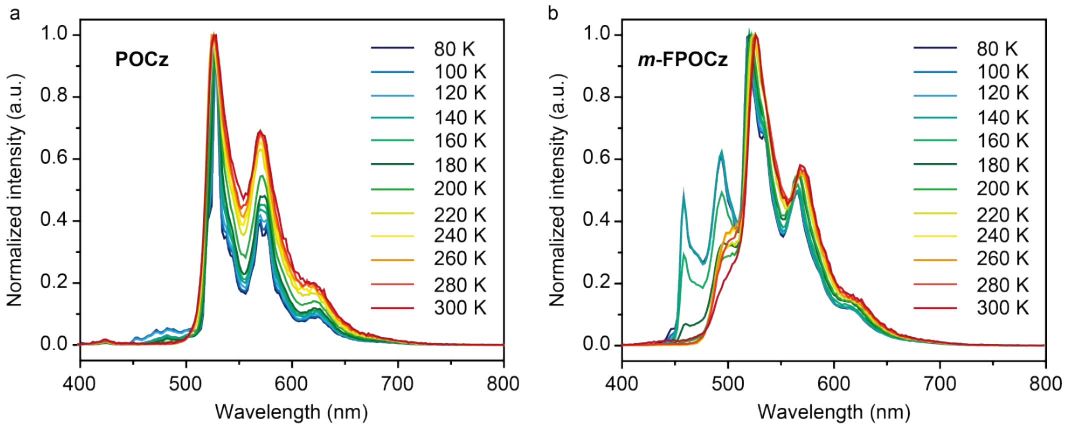

Figure S30. The normalized temperature-dependent afterglow spectra from 300 to 80 K of **POCz** (a) and ***m*-FPOCz** (b) crystals.

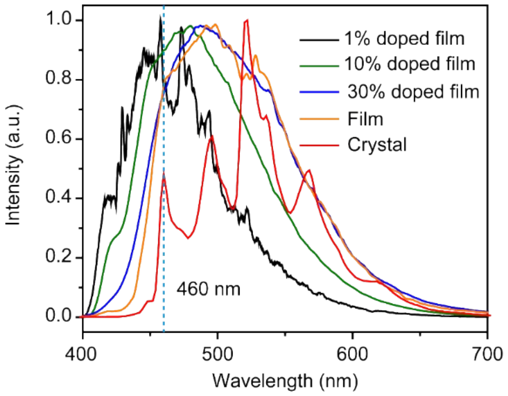

Figure S31. Phosphorescence spectra of ***m*-FPOCz** crystal, pure film and ***m*-FPOCz** (1, 10 and 30 wt%)-doped film in polymethyl methacrylate (**PMMA**), recorded following excitation at 365 nm at 80 K.

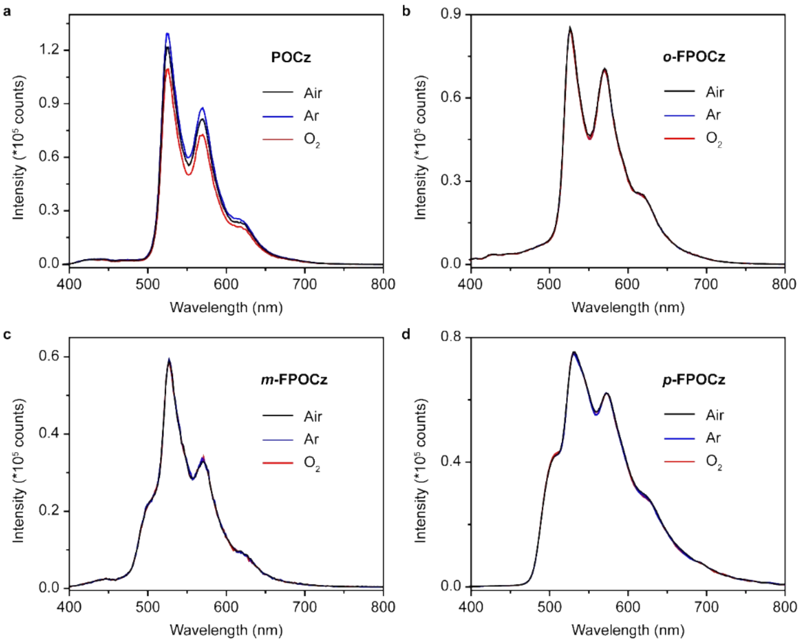

Figure S32. Organic afterglow spectra of **POCz** (a), ***o*-FPOCz** (b), ***m*-FPOCz** (c) and ***p*-FPOCz** (d) crystals excited by 365 nm in different atmosphere of air, Ar and O_2 at room temperature.

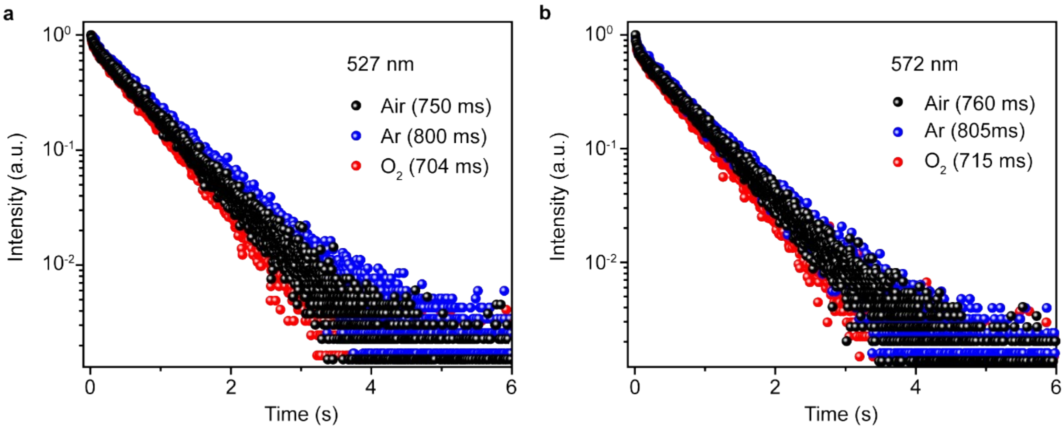

Figure S33. Organic afterglow decay profiles of the emission bands at 527 (a) and 572 nm (b) of **POCz** crystal excited by 365 nm in different atmosphere of air, Ar and O_2 at room temperature.

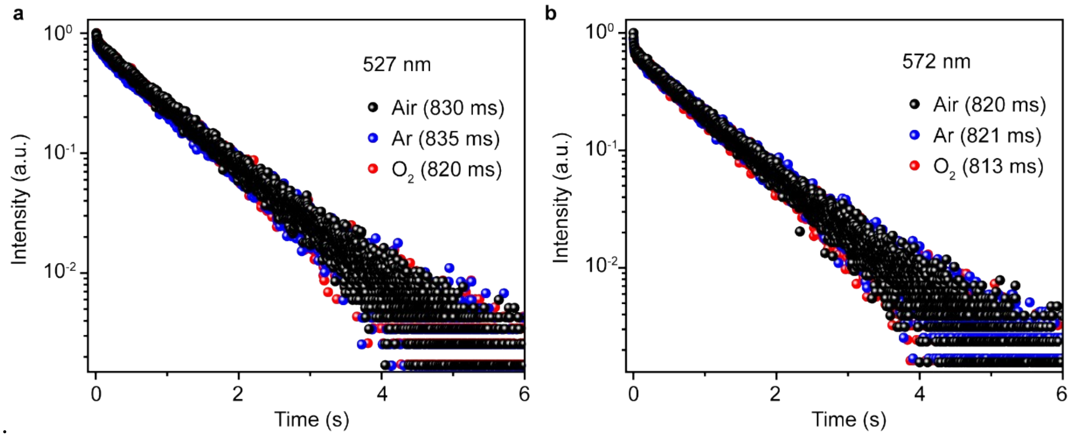

.

Figure S34. Organic afterglow decay profiles of the emission bands at 527 (a) and 572 nm (b) of ***o*-FPOCz** crystal excited by 365 nm in different atmosphere of air, Ar and O_2 at room temperature.

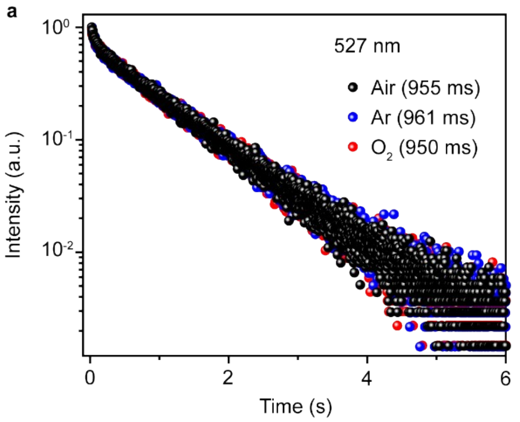

Figure S35. Organic afterglow decay profiles of the emission bands at 527 (a) and 572 nm (b) of ***m*-FPOCz** crystal excited by 365 nm in different atmosphere of air, Ar and O_2 at room temperature.

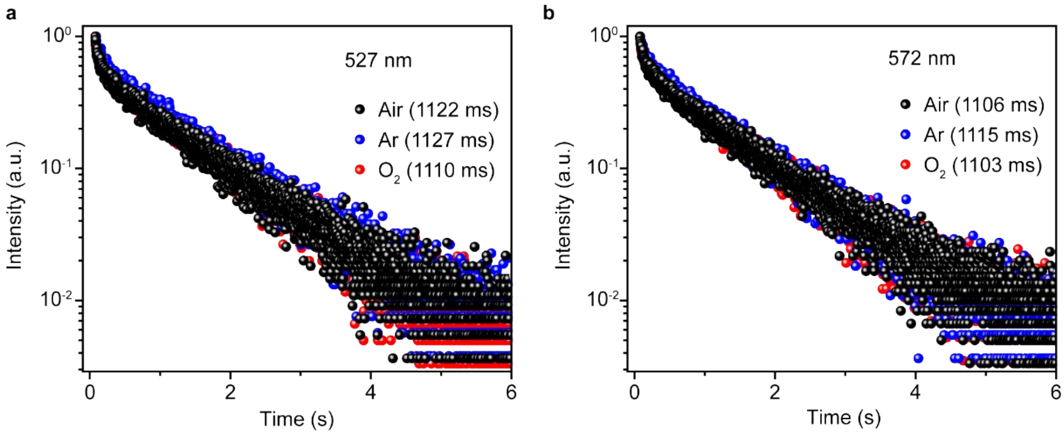

Figure S36. Organic afterglow decay profiles of the emission bands at 527 (a) and 572 nm (b) of ***p*-FPOCz** crystal excited by 365 nm in different atmosphere of air, Ar and O_2 at room temperature.

4. Single crystals analysis

Colorless single crystals of **POCz**, ***o*-FPOCz**, ***m*-FPOCz** and ***p*-FPOCz** were obtained by slow evaporation of a mixed dichloromethane and ethanol solution at room temperature. All the data of these single crystal structures were collected on a Bruker SMART APEX (II)-CCD at room temperature and crystal structures were analyzed by Mercury 4.0 software. Single crystal data were summarized in **Table S2**. The analyses of independent gradient model (IGM) for intermolecular weak interactions were carried out by Multiwfn 3.6 and were volume rendered by VMD 1.9.3 based on the crystal structures of **POCz**, ***o*-FPOCz**, ***m*-FPOCz** and ***p*-FPOCz**.

Table S2. Crystallographic data of **POCz**, ***o*-FPOCz**, ***m*-FPOCz** and ***p*-FPOCz** at room temperature.

Compound	**POCz**	***o*-FPOCz**	***m*-FPOCz**	***p*-FPOCz**
Formula	$C_{19}H_{13}NO$	$C_{19}H_{12}FNO$	$C_{19}H_{12}FNO$	$C_{19}H_{12}FNO$
Formula weight (g mol^{-1})	271.32	289.30	289.30	289.30
Crystal color	colorless	colorless	colorless	colorless
Wavelength (Å)	1.54178	0.71073	0.71073	0.71073
Crystal system	orthorhombic	orthorhombic	monoclinic	monoclinic
Space group	P-2	P-2	P-1	P-1
a, (Å)	17.214 (2)	11.8585 (9)	14.608 (3)	8.9406 (17)
b, (Å)	14.4042 (16)	10.3783 (7)	5.4287 (11)	22.597 (4)
c, (Å)	5.5668 (7)	22.8559 (16)	18.371 (4)	7.0302 (12)
α, (deg)	90	90	90	90
β, (deg)	90	90	107.996 (5)	91.313 (5)
γ, (deg)	90	90	90	90
volume, (Å^3)	1380.3 (3)	2812.9 (3)	1385.5 (5)	1419.9 (4)
Z	4	8	4	4
Density, (g cm^{-3})	1.306	1.366	1.387	1.353
μ, (mm^{-1})	0.636	0.094	0.095	0.093

F(000)	568	1200	600	600
$h_{\max}$, $k_{\max}$, $l_{\max}$	20, 17, 5	11, 13, 30	19, 7, 24	10, 30, 9
$Theta_{\max}$	27.875	28.206	28.206	28.217
CCDC number	149367	1975648	1975612	1975625

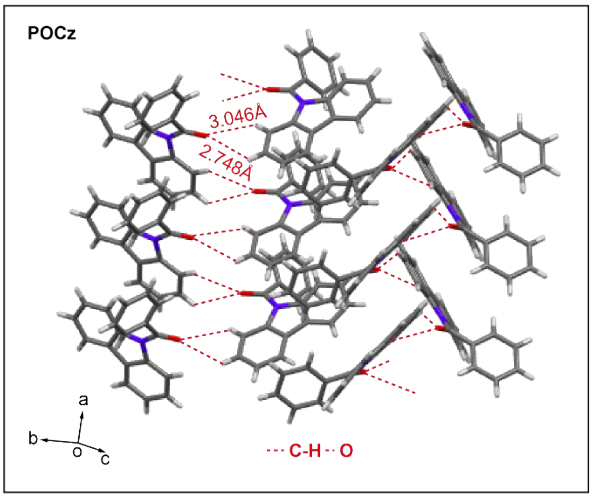

Figure S37. Molecular packing arrangements showing detailed intermolecular interactions of in **POCz** single crystal.

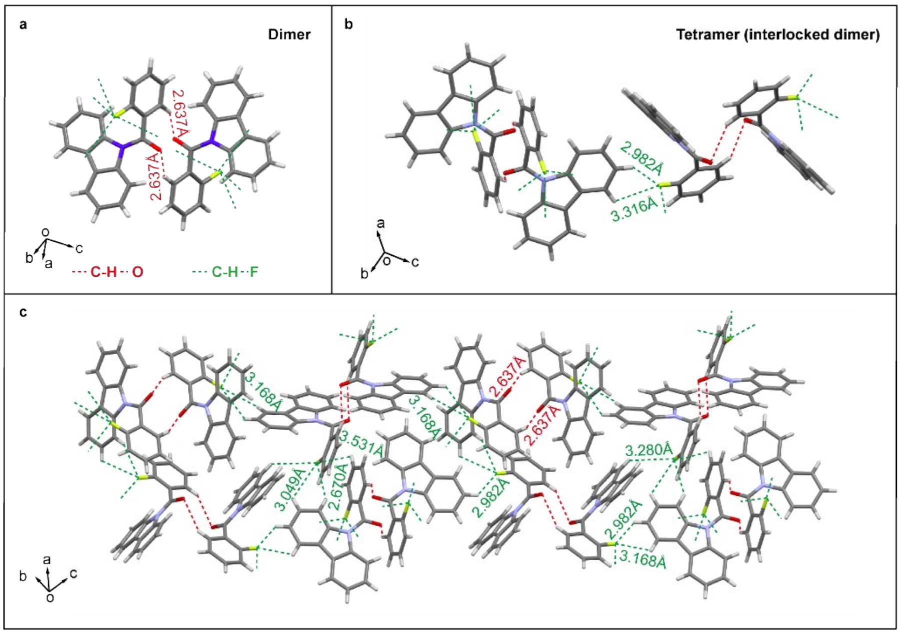

Figure S38. Dimer (a), tetramer (b) and molecular packing arrangements (c) showing detailed intermolecular interactions in ***o*-FPOCz** single crystal.

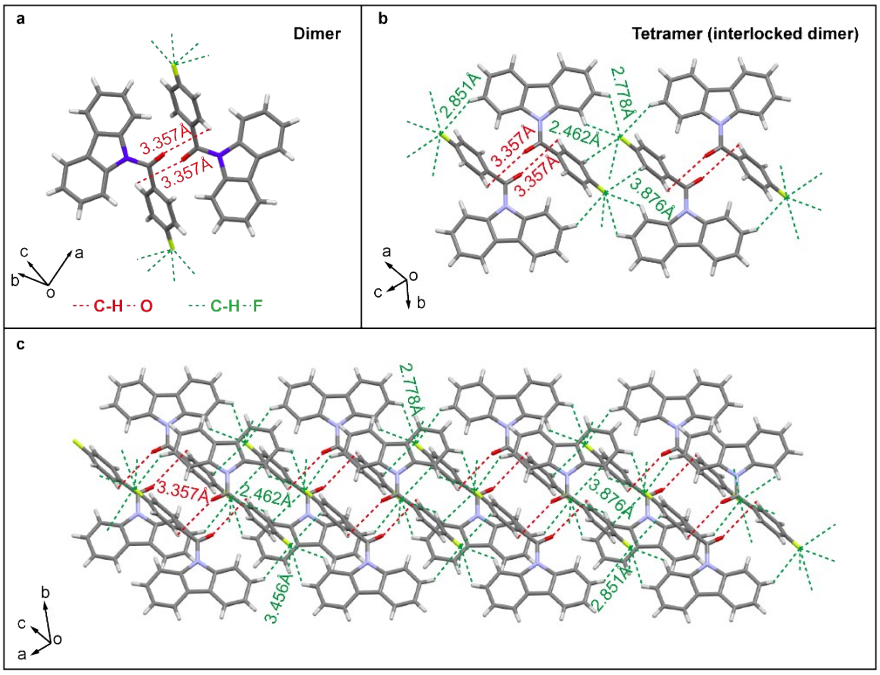

Figure S39. Dimer (a), tetramer (b) and molecular packing arrangements (c) showing detailed intermolecular interactions in ***p*-FPOCz** single crystal.

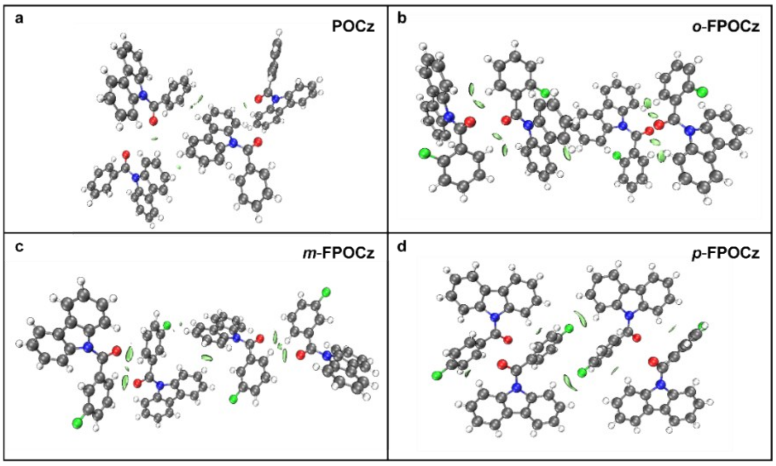

Figure S40. The calculated intermolecular interactions (green isosurface) of selected dimers extracted from **POCz** (a), ***o*-FPOCz** (b), ***m*-FPOCz** (c) and ***p*-FPOCz** (d) single crystals (the isovalue is 0.01).

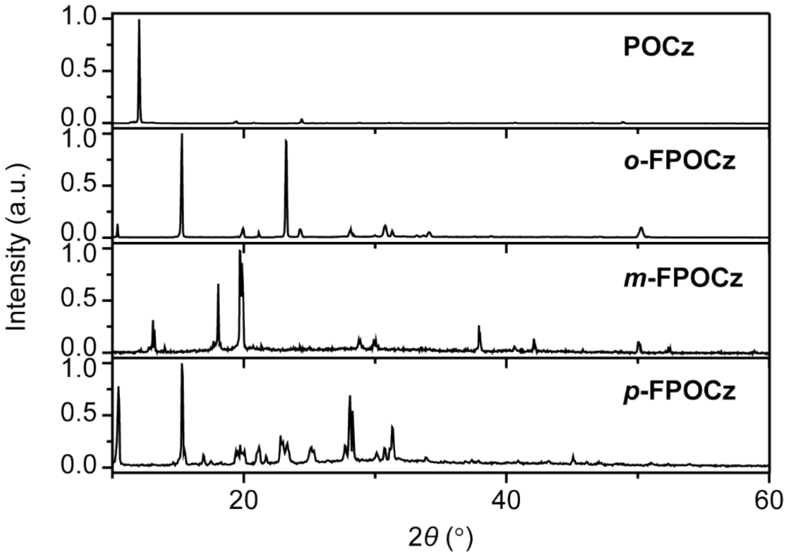

Figure S41. XRD spectra of **POCz** and ***o*/*m*/*p*-FPOCz** crystals.

Aggregation structures have great influence on the photophysical properties of organic optoelectronic materials. Particularly, H-aggregation plays a vital role in stabilizing the excited triplet excitons for achieving the organic afterglow emission in the crystalline states[4, 5]. The presence of H-aggregation can be verified by Frenkel exciton theory based on the single crystal structures of **POCz**, ***o*-FPOCz**, ***m*-FPOCz** and ***p*-FPOCz**, where the exciton splitting energy ($\Delta\varepsilon$) of the selected dimer can be simulated by:

$$\Delta\varepsilon = \frac{2|M|^2}{r_{uv}^3}\left(\cos\alpha - 3\cos\theta_1\cos\theta_2\right)$$

where M is the transition moment that can be simulated by TD-DFT simulation, r_{uv} is the intermolecular distance between the selected dimer, α is the angle between the transition dipole moments, θ_1 and θ_2 are angles between transition dipole moments of the two molecules and the interconnection of their molecular centers. When $\Delta\varepsilon > 0$, it is H-aggregation, and when $\Delta\varepsilon < 0$, it belongs to J-aggregation.

Table S3. H-aggregates in **POCz**, ***o*-FPOCz**, ***m*-FPOCz** and ***p*-FPOCz** single crystals identified by the positive exciton splitting energy ($\Delta\varepsilon$).

Compound	H-aggregate	*a* (°)	θ_1 (°)	θ_2 (°)	M (Debye)	*r* (Å)	$\Delta\varepsilon$ (eV)
POCz	H1	175.5	52.8	131.2	1.82	10.38	0.000733
	H2	175.5	48.8	127.2	1.82	10.38	0.000733
	H3	0.0	74.8	74.8	1.82	5.57	0.019
	H4	0.0	105.2	105.2	1.82	5.57	0.019
***o*-FPOCz**	H1	60.4	40.5	84.8	0.65	7.95	0.000298
	H2	60.4	95.2	139.5	0.65	7.95	0.000298
	H3	69.6	30.4	86.9	0.65	7.35	0.000276
	H4	69.6	93.1	149.6	0.65	7.35	0.000276
	H5	69.6	92.9	31.9	0.65	8.43	0.000415
	H6	69.6	148.1	87.1	0.65	8.43	0.000415
	H7	0.0	124.8	124.8	0.65	11.86	0.000002
	H8	110.4	102.2	18.9	0.65	9.20	0.000167
	H9	110.4	161.1	77.8	0.65	9.20	0.000167
***m*-FPOCz**	H1	0.0	62.0	62.0	1.96	5.43	0.0102
	H2	0.0	118.0	118.0	1.96	5.43	0.0102
	H3	180.0	28.3	151.7	1.96	11.45	0.00425
	H4	180.0	127.9	52.1	1.96	7.48	0.00151
	H5	180.0	143.9	36.1	1.96	8.84	0.00668
	H6	180.0	132.5	47.5	1.96	12.97	0.000817
***p*-FPOCz**	H1	0.0	70.0	70.0	0.81	11.25	0.000372
	H2	0.0	109.9	109.9	0.81	7.03	0.00154
	H3	0.0	70.1	70.1	0.81	7.03	0.00154
	H4	0.0	110.0	110.0	0.81	11.25	0.000372
	H5	180.0	16.9	163.1	0.81	6.64	0.00487
	H6	180.0	28.7	151.3	0.81	9.96	0.00108
	H7	79.5	136.4	66.5	0.81	7.33	0.00217
	H8	79.5	113.5	43.6	0.81	7.33	0.00217

5. Theoretical calculations

Density functional theory (DFT) and time-dependent DFT (TD-DFT) simulations were performed on the Gaussian 09 package. The ground state geometries were optimized by DFT method of Becke's three-parameter exchange functional along with the Lee Yang Parr's correlation functional (B3LYP)/6-31G(d). The optimized static point was further carried out by harmonic vibration frequency analysis to guarantee that the real local minimum was achieved. The excitation energy of the *n*-th singlet state (S_n) and the *n*-th triplet state (T_n) states were calculated by TD-DFT method of B3LYP/6-31G(d) based on the optimized structure at ground state (S_0). Dalton program with quadratic response function method was used to predict spin-orbit coupling (SOC) matrix elements between the singlet excited states and triplet excited states. The single molecular SOC values of **POCz**, ***o*-FPOCz**, ***m*-FPOCz** and ***p*-FPOCz** were carried out using B3LYP functional and cc-pVDZ basis set on the basis of the optimized geometry of the lowest triplet excited state (T_1).

Table S4. TD-DFT predicted singlet and triplet excited state energies and transition configurations of **POCz**.

Excited state	*n*-th	Energy (eV)	Transition configuration (%)
S_n	1	3.8193	H-1→L (5.31), H→L (93.07)
T_n	1	3.1454	H-6→L+5 (3.58), H-2→L+1 (2.48), H-1→L (11.38), H-1→L+1 (62.7), H-1→L+2 (2.21), H→L+3 (8.53)
	2	3.2840	H-3→L (2.24), H→L (82.85), H→L+4 (4.64)
	3	3.4359	H-5→L+4 (2.04), H-4→L (2.94), H-4→L+2 (11.71), H-3→L (62.07), H-3→L+4 (2.5), H-2→L (5.2), H-2→L+2 (2.96), H→L (2.02)
	4	3.6712	H-2→L+3 (2.72), H→L (3.98), H→L+1 (81.06)
	5	3.7356	H-1→L (79.97), H-1→L+1 (11.7), H-1→L+4 (2.08)
	6	3.9575	H-5→L (43.26), H-4→L (8.38), H-4→L+2 (7.1), H-3→L (5.81), H-2→L (18.91)
	7	4.1616	H-5→L (4.39), H-3→L (2.47), H-2→L (6.88), H-2→L+1 (7.79), H-2→L+4 (3.18), H-1→L+1 (17.93), H→L+3 (35.69), H→L+4 (9.5)
	8	4.2398	H-5→L (14.37), H-4→L (56.38), H-4→L+4 (2.07), H-3→L+2 (3.6), H-2→L (6.54), H→L+3 (3.93)
	9	4.3023	H-6→L+1 (10.75), H-4→L (2.02), H-2→L (2.13), H-2→L+3 (9.52), H-2→L+4 (2.31), H-1→L+3 (7.79), H-1→L+5 (12.21), H→L (4.97), H→L+1 (7.9), H→L+3 (3.89), H→L+4 (17.92), H→L+6 (5.76)
	10	4.5088	H-5→L (14.8), H-4→L+1 (2.59), H-4→L+2 (38.72), H-3→L (12.22), H-2→L+1 (8.79), H-2→L+2 (8.19), H→L+2 (4.26)

Table S5. TD-DFT predicted singlet and triplet excited state energies and transition configurations of ***o*-FPOCz**.

Excited state	*n*-th	Energy (eV)	Transition configuration (%)
S_n	1	3.8149	H-1→L (98.24)
T_n	1	3.1214	H-5→L+5 (3.6), H-2→L+1 (2.97), H-2→L+3 (2.23), H-1→L (18.96), H-1→L+1 (56.55), H→L+4 (8.73)
	2	3.2888	H-2→L+4 (2.74), H→L (81.2), H→L+3 (5.17)
	3	3.5049	H-6→L (3.94), H-6→L+2 (3), H-6→L+3 (2), H-4→L (26.1), H-4→L+2 (7.98), H-3→L (36.1), H-3→L+2 (5.79), H-3→L+3 (6.37), H-2→L (3.12)
	4	3.7071	H-5→L+1 (2.47), H-2→L+4 (5.11), H→L (4.25), H→L+1 (77.91), H→L+3 (2.38)
	5	3.7524	H-1→L (70.32), H-1→L+1 (17.93), H-1→L+3 (2.93), H→L+1 (2.57)
	6	4.0423	H-6→L (24.14), H-4→L (39.58), H-4→L+2 (3.14), H-3→L (4.38), H-3→L+3 (7.61), H-2→L (9.45)
	7	4.1512	H-6→L (14.32), H-6→L+2 (2.42), H-4→L (8.65), H-4→L+2 (16.25), H-3→L (48.25), H-3→L+2 (6.18)
	8	4.1817	H-4→L (3.38), H-2→L (6.18), H-2→L+1 (10.61), H-2→L+3 (5.63), H-1→L+1 (17.87), H→L+4 (45.42)
	9	4.3134	H-5→L+1 (10.77), H-2→L+4 (11.91), H-1→L+4 (10.18), H-1→L+5 (11.24), H→L (6.42), H→L+1 (9.94), H→L+2 (6.21), H→L+3 (16.95), H→L+6 (5.88)
	10	4.5334	H-4→L (5.65), H-3→L+2 (2.67), H-2→L (28.12), H-2→L+1 (36.55), H-1→L (2.52), H-1→L+2 (2.02), H-1→L+3 (4.96), H-1→L+4 (2.58), H→L+5 (5.28)

Table S6. TD-DFT predicted singlet and triplet excited state energies and transition configurations of ***m*-FPOCz**.

Excited state	*n*-th	Energy (eV)	Transition configuration (%)
S_n	1	3.7443	H-1→L (98.4)
T_n	1	3.1366	H-6→L+5 (3.47), H-1→L (12.09), H-1→L+1 (62.27), H→L+3 (5.6), H→L+4 (4.21)
	2	3.2332	H→L (83.42), H→L+4 (3.14)
	3	3.4249	H-5→L (2.67), H-4→L (20.43), H-4→L+2 (4.5), H-3→L (23.97), H-2→L (26.71), H-2→L+2 (6.18), H→L (2.13)
	4	3.6680	H-1→L (74.49), H-1→L+1 (10.85), H→L+1 (6.19)
	5	3.6945	H-1→L (6.87), H→L (2.38), H→L+1 (75.62), H→L+2 (2.83)
	6	3.9133	H-5→L (34.47), H-4→L (3.72), H-4→L+2 (9.35), H-2→L (33.63), H-2→L+2 (4.73)
	7	4.0790	H-5→L (25.41), H-4→L (51.41), H-2→L (9.02), H-2→L+4 (2.03)
	8	4.1688	H-3→L (9.61), H-3→L+1 (5.74), H-3→L+3 (2.36), H-2→L+1 (2.87), H-1→L+1 (18.28), H→L+3 (23.79), H→L+4 (22.77)
	9	4.2775	H-6→L+1 (10.54), H-3→L+3 (5.36), H-3→L+4 (3.7), H-2→L+3 (3.07), H-2→L+4 (2.83), H-1→L+3 (4.51), H-1→L+4 (3.13), H-1→L+5 (11.98), H→L (5.46), H→L+1 (9.65), H→L+3 (11.35), H→L+4 (11.13), H→L+6 (5.66)
	10	4.4760	H-5→L (12.74), H-4→L (5.17), H-4→L+2 (8.23), H-3→L (10.47), H-3→L+2 (11.96), H-2→L+1 (13.87), H-2→L+2 (28.3)

Table S7. TD-DFT predicted singlet and triplet excited state energies and transition configurations of ***p*-FPOCz**.

Excited state	*n*-th	Energy (eV)	Transition configuration (%)
S_n	1	3.8090	H-1→L (6.14), H→L (92.19)
T_n	1	3.1444	H-6→L+5 (3.05), H-1→L (11.07), H-1→L+1 (57.53), H-1→L+2 (7.59), H→L+3 (9.42)
	2	3.2760	H→L (83.23), H→L+4 (4.57)
	3	3.4270	H-5→L+2 (3.29), H-4→L+2 (6.59), H-3→L (38.83), H-3→L+4 (2.7), H-2→L (35.13), H→L (2.04)
	4	3.6702	H→L (3.93), H→L+1 (75.34), H→L+2 (7.66)
	5	3.7232	H-1→L (80.22), H-1→L+1 (10.85), H-1→L+4 (2.24)
	6	3.9907	H-6→L (3.19), H-5→L (27.35), H-4→L (33.93), H-4→L+2 (4.23), H-2→L (12.66), H-2→L+4 (2.48)
	7	4.1596	H-5→L (2.14), H-3→L (4.65), H-3→L+1 (4.69), H-3→L+4 (3.66), H-2→L (2.74), H-2→L+1 (4.48), H-1→L+1 (17.87), H→L+3 (41.82), H→L+4 (4.88)

	8	4.2995	H-6→L+1 (9.02), H-5→L (2.7), H-5→L+1 (2.37), H-3→L+3 (6.87), H-2→L+3 (7.31), H-1→L+3 (7.96), H-1→L+5 (12.76), H→L (4.81), H→L+1 (8.39), H→L+3 (3.08), H→L+4 (19.2), H→L+6 (5.41)
	9	4.4236	H-6→L (3.97), H-5→L (15.28), H-5→L+2 (6.14), H-4→L (25.74), H-4→L+2 (3.05), H-3→L (8.07), H-3→L+2 (9.54), H-2→L+1 (7.38), H-2→L+2 (9.93)
	10	4.4631	H-6→L (2.98), H-6→L+2 (3.4), H-5→L (11.39), H-5→L+1 (2.75), H-5→L+2 (5.79), H-4→L+1 (7.07), H-4→L+2 (25), H-3→L (8.4), H-3→L+1 (3.13), H-3→L+2 (4.49), H→L+2 (15.42)

Table S8. Theoretically calculated S_1-T_n energy gap and the SOC constants between S_1 and T_n of **POCz**, ***o*-FPOCz**, ***m*-FPOCz** and ***p*-FPOCz**.

	S_1-T_n energy gap				**SOC**			
S_1/T_n	**POCz**	***o*-FPOCz**	***m*-FPOCz**	***p*-FPOCz**	**POCz**	***o*-FPOCz**	***m*-FPOCz**	***p*-FPOCz**
S_1/T_1	0.67	0.69	0.61	0.66	0.62	1.14	1.89	1.48
S_1/T_2	0.53	0.53	0.51	0.53	2.10	0.57	4.99	0.37
S_1/T_3	0.38	0.31	0.32	0.38	0.14	0.19	14.94	0.44
S_1/T_4	0.15	0.11	0.08	0.14	0.06	0.22	11.92	0.42
S_1/T_5	0.08	0.06	0.05	0.09	0.42	0.26	0.58	0.33
S_1/T_6	-0.14	-0.23	-0.17	-0.18	0.47	0.86	1.83	0.90
S_1/T_7	-0.34	-0.34	-0.33	-0.35	0.16	0.45	0.39	0.35
S_1/T_8	-0.42	-0.37	-0.42	-0.49	10.24	0.48	7.70	0.78
S_1/T_9	-0.48	-0.50	-0.53	-0.61	0.03	1.02	0.81	1.54
S_1/T_{10}	-0.69	-0.72	-0.73	-0.65	0.68	1.48	0.68	0.84

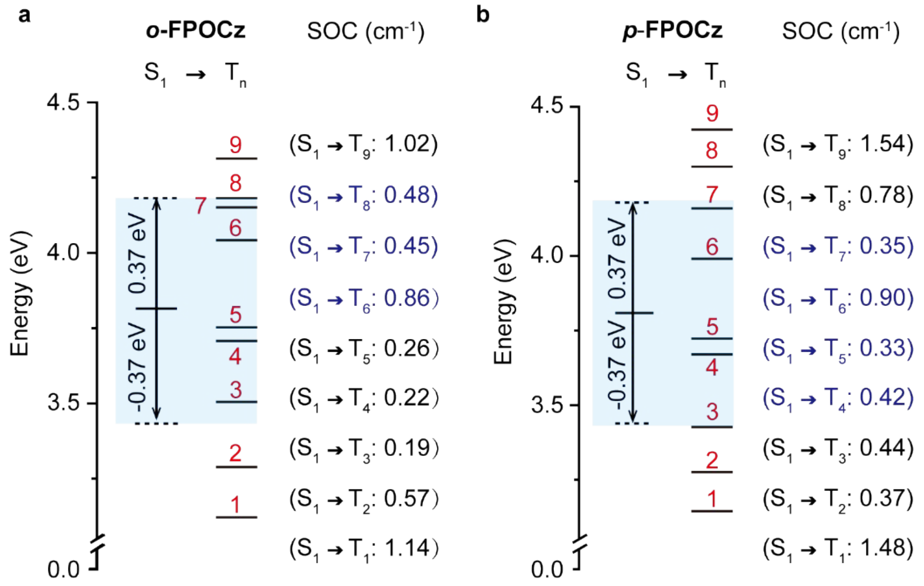

Figure S42. TD-DFT calculated energy level diagram and the corresponding SOC constants of ***o*-FPOCz** (a) and ***p*-FPOCz** (b).

6. Quick response code fabrication

The flexible quick response (QR) code can be easily fabricated by screen printing. Firstly, the yellow code was screen printed on a transparent polyethylene terephthalate (PET) substrate using a mixture of ***p*-FPOCz** powder and ALOE VERA gel (~ 30 mg/mL) as the gel ink, then the blue background and top red code were printed on another PET substrate, respectively. Finally, the multilayer QR code was arranged in the order of red, blue and yellow layers. The top red code could be easily observed and detected with the information of “NJUPT” under ultraviolet light excitation. The bottom code layer with white emission under UV light excitation is virtually invisible because of the background fluorescence interference induced by the middle blue background layer. Notably, when the UV light is turned off, the bottom yellow QR code immediately appears and can be readily read by the commercial mobile phone because of the extraordinary organic afterglow nature of ***p*-FPOCz**, thus showing the encrypted information of “COO”.

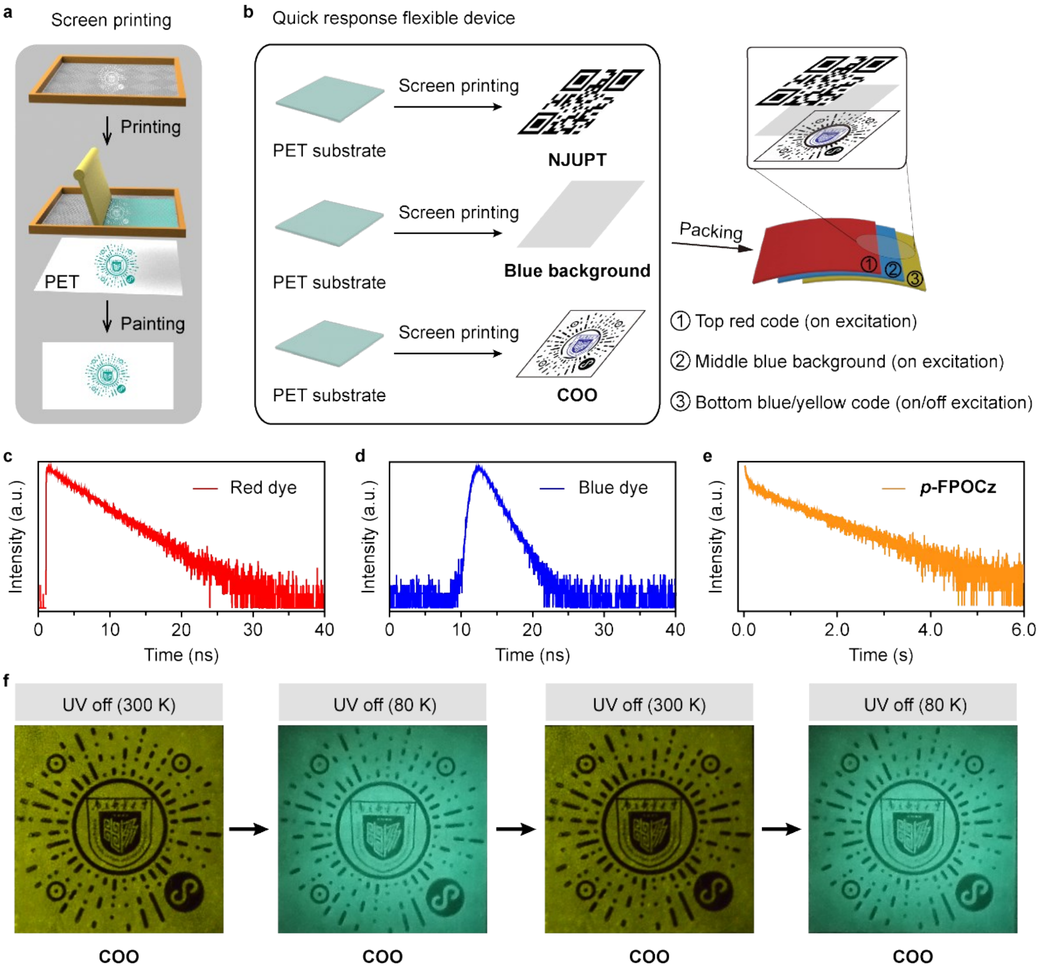

Figure S43. Modeling of screen printing process adopted for patterning (a) and fabrication procedures (b) of QR code. (c-e). Lifetime decay profiles of red (c), blue (d) dyes and ***p*-FPOCz** (e). (f). Photographs of multiplexing encryption QR code under 365 nm irradiation at different temperature.

References:

1. Y. Tao, R. Chen, H. Li, J. Yuan, Y. Wan, H. Jiang, C. Chen, Y. Si, C. Zheng, B. Yang, G. Xing and W. Huang, *Adv. Mater.*, 2018, **30**, 1803856.
2. Z. An, C. Zheng, Y. Tao, R. Chen, H. Shi, T. Chen, Z. Wang, H. Li, R. Deng, X. Liu and W. Huang, *Nat. Mater.*, 2015, **14**, 685.
3. J. Yuan, Y. Wang, L. Li, S. Wang, X. Tang, H. Wang, M. Li, C. Zheng and R. Chen, *J. Phys. Chem. C*, 2020, **124**, 10129.
4. S. Hirata, *Adv. Opt. Mater.*, 2017, **5**, 1700116.
5. J. Yuan, S. Wang, Y. Ji, R. Chen, Q. Zhu, Y. Wang, C. Zheng, Y. Tao, Q. Fan and W. Huang, *Mater. Horiz.*, 2019, **6**, 1259.